

An advanced aero-thermodynamic study of a heart-shaped dimpled pipe

Muhsin Can Akkurt^{1,2*}, Marco Virgilio³, Tony Arts², Kevin M. Van Geem¹, Delphine Laboureur²

¹Ghent University, Laboratory for Chemical Technology, Technologiepark 125, 9052 Gent, Belgium

²The von Karman Institute for Fluid Dynamics, Waterloosesteenweg 72, B-1640 Sint-Genesius Rode, Belgium

³University of Southampton, Faculty of Engineering and Physical Science, Boldrewood Campus, UK

*Corresponding author: Muhsin Can Akkurt, E-mail: mcakkurt@gmail.com

Contributing authors: Marco Virgilio (m.virgilio@soton.ac.uk); Tony Arts (tony.arts@vki.ac.be); Kevin M. Van Geem (kevin.vangeem@ugent.be); Delphine Laboureur (delphine.laboureur@vki.ac.be)

Abstract

The detailed flow field and local heat transfer enhancement in a pipe with heart-shaped dimples on the internal surface were experimentally studied. The flow structures were investigated at a flow regime of $Re=20k$ in five different measurement planes around a dimple in the streamwise and spanwise directions using both planar PIV and stereo PIV. A ray tracing-based image correction method was utilized to overcome the important image distortions caused by the optically complex geometry of the dimple for the planar PIV measurements. Furthermore, the convective heat transfer coefficient on the wall of the dimple was investigated utilizing steady-state liquid crystal thermography (LCT) and infrared thermography within the flow regime range of $Re=20k-60k$. A comprehensive uncertainty analysis was conducted to account for the multiple measured quantities and corresponding error sources on such a complex geometry. The resulting heat transfer and flow fields revealed that maximum heat transfer enhancement is concentrated along the reattachment line downstream of the dimple where higher kinetic energy levels are observed. The enhancement factor, which is a measure of the heat transfer improvement relative to a smooth pipe, was evaluated on average at 1.7 across the dimpled surface, with local maxima reaching values up to 2.8. The dimpled pipe under examination had a relative skin friction coefficient of approximately 1.8 compared to a smooth pipe. This outperforms some of the roughness elements, such as ribs and spherical dimples, previously studied on similar circular channels in literature.

Keywords: Roughened channels, dimples, heat transfer, liquid crystals thermography, particle image velocimetry, ray tracing

1 Introduction

Heat transfer enhancement techniques in channel flows are widely employed in modern industrial applications. A variety of roughness elements are implemented in the channels to maximize the

convective heat transfer between the flow and the surrounding walls. Heat transfer enhancement is provided by promoting turbulence and disturbing the boundary layer to be separated and subsequently reattached downstream of the corresponding element [1].

This same advantage is also beneficial for large scale endothermic chemical processes that are carried out in gas fired furnaces. A recent example is the implementation of 3-dimensional roughness elements in steam cracking reactors' tubes, resulting in reduced internal wall temperatures. This "cooling effect" decreases the rate of coke formation which causes a decrease in the heat transfer from the furnace to the process gas and an increase in the pressure drop across the channel. When one of these negative consequences becomes too big, the operations need to be halted for reactor decoking. Therefore, further heat extraction enhancements can improve process economics preventing additional production interruptions caused by the decoking process [2].

However, besides heat transfer enhancement, the utilization of these roughness elements induces additional pressure losses in the channels. As these losses lead to additional compression power for heat exchangers and negative effects on the selectivity of the required products in reactors, the trade-off between improved heat transfer and greater pressure penalties must be carefully considered in the element selection.

Ligrani [1] stated that dimpled surfaces cause relatively low friction factors in comparison to other elements since they do not protrude into the flow field while improving the overall heat transfer. In another study, Afanasyev et al. [3] showed that spherical cavities on flat plates increase the heat transfer by 30-40% without a significant increase in skin friction. Burgess and Ligrani [4] studied the influence of dimple geometries on the flow structure and heat transfer where three different dimple depth ratios (dimple depth to dimple print) are investigated. Experimental results showed that the Nusselt number and friction factor increase as the dimple depth increases because deeper dimples provide an increase in turbulence production with stronger secondary flows ejected and more intense vortices. The outcome was supported in another study [5] where the authors investigated dimpled surfaces in a rectangular channel. The results revealed that as the dimple depth ratio increases, much larger recirculation vortices are situated within dimples. The turbulence intensity is substantially increased, particularly in the downstream region where the local heat transfer is improved, leading to the improvement in global heat transfer despite a larger pressure penalty. Xie et al. [6] compared teardrop-shaped dimples with different eccentricities with

spherical dimples in a numerical investigation where a k- ϵ turbulent model is coupled with an enhanced wall function. The outcome demonstrates that in the teardrop dimple with positive eccentricity compared to the spherical dimple, the flow easily covers the dimple surface and impinges the downstream portion with higher energy. They found that the intended performance of the dimpled surface increases with the eccentricity in the investigated range. A maximum performance was observed when the ratio of eccentricity to the hydraulic diameter, e/D_h , was equal to 0.4.

Zhou et al. [8] examined turbulent flow structures in detail over a dimpled plate via particle image velocimetry (PIV) measurements. Along with the vortices shed from the spherical dimples, the authors managed to quantitatively reveal the Reynolds stresses and turbulent kinetic energy over the dimpled surface. Unfortunately, a heat transfer investigation was not included. One of the few studies focusing on dimples employed inside a circular channel was conducted by Bunker and Donnellan [9]. The heat transfer coefficient was determined by means of steady-state liquid crystals without investigating the flow field. Since no spatially resolved heat transfer coefficient data was provided, the interpretation of the relation between the flow structures and heat transfer is not possible. Zheng et al. [24] comprehensively investigated the turbulent flow structures over a micro-rib dimple-structured surface by combining the pressure transducer measurements and PIV. Moreover, the flow field was successfully correlated with the heat transfer measurements carried out by means of LCT. However, the survey was carried out in a rectangular channel with one dimpled surface and lacked a circumferential dimple arrangement as in a tubular pipe. Virgilio et al. [10] used steady-state liquid crystals thermography (LCT) and PIV to characterize both heat transfer and flow field phenomena in a half-dimpled pipe. The authors provided detailed spatially resolved experimental data around a spherical dimple along with the friction factors across the tube at the flow regime range $Re=20k-80k$. However, Virgilio et al. did not report the flow field on the symmetry line of the half tube with spherical dimples due to the lack of optical access.

Several numerical studies were also carried out to optimize the dimple shape by maximizing the heat transfer and minimizing the pressure loss. Chen et al. [7] found that an asymmetric dimple of which the deepest point of the spherical indentation is skewed in the downstream flow direction results in a considerably higher heat transfer compared to the spherical dimple with no additional pressure penalty. Dedeyne et al. [2] carried out an optimization study with multiple design parameters such as width, height and curvature to obtain a dimple geometry to be used in steam

cracking reactors. The study revealed that heart-shaped dimples lower the pressure drop penalty by 20% compared to spherical dimples when utilized in circular channels because they result in more stable vortex structures. However, these numerical and optimization studies there were not experimentally validated. This is essential so that the simulations can be used to generate and evaluate even more advanced designs. Moreover, although several experimental studies were conducted to understand the flow and heat transfer phenomena across dimples in literature, the number of quantitative examinations of the aerothermodynamic characteristics is quite limited, especially when the dimples with optically complex shape are implemented in circular channels.

The preceding literature review shows that spatially resolved experimental data on circular channels with optimized dimples, such as teardrop, heart-like shapes, due to their optically complex geometries are still lacking. In the current study we want to resolve this and provide detailed heat transfer and flow field data that can be used to validate the flow and heat transfer characteristics in a circular channel with heart-shaped dimples, as they have demonstrated promising performance for tubular steam cracking reactors, according to the work of Dedeyne et al. [2]. The heat transfer measurements are carried out by means of steady-state LCT and an infrared camera to define spatially resolved convective heat transfer coefficient fields. As the technique includes several separate measurements and therefore uncertainty sources, a comprehensive pixel-wise uncertainty analysis is carried out, which the literature lacks for such dimple surfaces. Complete enhancement factor (EF) distributions across three dimples at different locations were obtained in the range of $Re=20k-60k$. The flow field measurements were carried out by PIV for five different planes in the streamwise and the spanwise directions inside a heart-shaped dimple at the flow regime $Re=20k$. Stereoscopic PIV was employed to investigate the three velocity components in the spanwise directions, while turbulent characteristics in streamwise direction planes were investigated via planar PIV where the ray tracing assisted calibration [11, 12] was employed. The results were compared with the performances of various roughness elements, such as ribs and spherical dimples implemented in similar circular channels, reported in literature [10, 13].

2 Experimental Setup

2.1 Test geometry

In this study, the dimple shapes proposed in the optimization study of Dedeyne et al. [2] were examined via both heat transfer and flow field measurements. Optimizing the width, length, and curvature across the dimple to achieve maximal heat transfer enhancement with minimal pressure drop resulted in the heart-shaped dimple illustrated in Figure 1a. The dimpled half of the test geometry (Figure 1b) was established by forming these complex shaped dimples on the internal surface of a smooth pipe with a length of 990 mm and an inner diameter of 150 mm. The test geometry was manufactured by a vacuum casting technique with a transparent ABS-like polyurethane material. To ensure appropriate optical access to the pipe's interior, the geometry consists of a transparent dimpled and smooth half. The former was designed with ten dimple rows that were positioned in an in-line layout, as depicted in Figure 1b. Each row includes five indentations with a maximum depth of 4.2 mm and a width 40 mm. The indentations were positioned around the half circumference with a 36-degree angular offset, leading 2mm apart in-between two adjacent dimples. The distance from the leading edge of a dimple to the following leading edge in streamwise direction is 80mm.

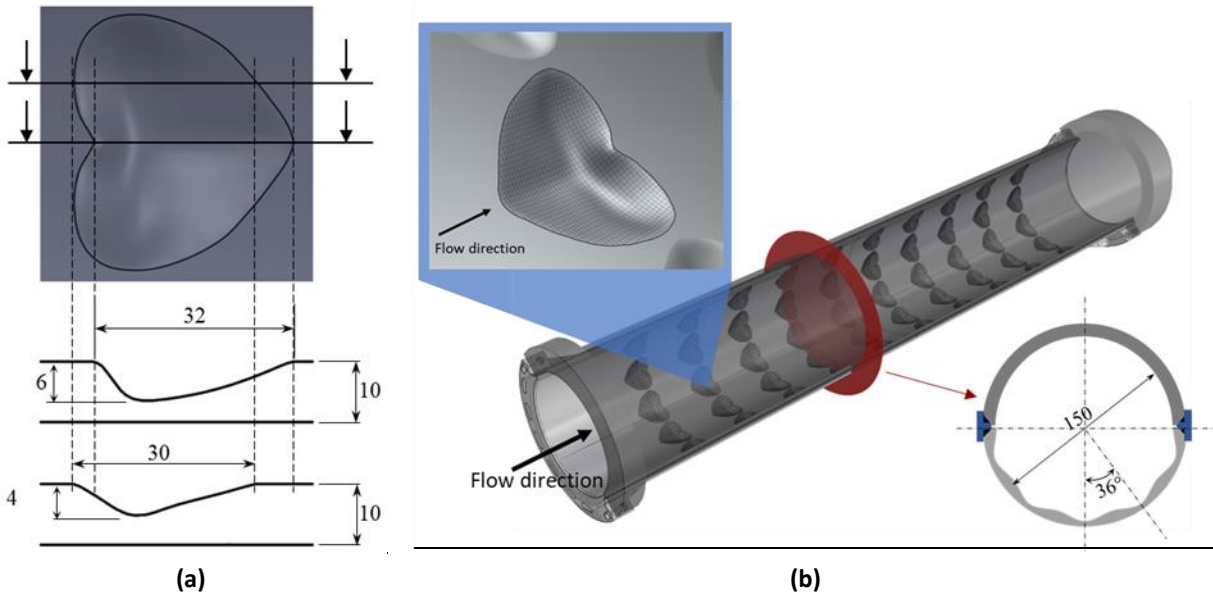


Figure 1: The heart shaped dimple (a) and the dimple rows placed on the test geometry (b)

2.2 Heat transfer measurements

2.2.1 Experimental configuration and calibrations

The heat transfer across the channel geometry was investigated within the flow regime of $Re=20000-60000$ through an open circuit low-speed facility which is operating with air. The side view of the test channel (Figure 2a) shows the measurement configuration allowing an SLR (single-lens reflex) camera, Nikon D7100, to record the internal surface during the measurements while an infrared camera (FLIR A655sc) simultaneously to measure the outer surface temperature for the same field of view. The details of the facility, designed to study the heat transfer field and pressure drops across circular channels, and the detailed concept of the measurement configuration can be found in the previous studies [10,13].

For the internal wall temperature measurements, a coating of thermo-chromic liquid crystals (LCRHallcrest-SPN100, changing color in response to temperature variations in the range of around $33-55^{\circ}\text{C}$) with thickness of 10 microns was applied to the internal surfaces of the dimpled half. To improve the color contrast, a layer of black paint (LCRHallcrest-SPB100) was applied to the internal surface on the top of the liquid crystal layer (Figure 2b). The internal surface of the smooth half was also painted black without applying any liquid crystal layer to increase its emissivity value to approximately 1, resulting in an assumption of negligible heat transfer to the opposing surface via radiation. To generate a uniform heat flux, a transparent conductor film (Holland Shielding Systems, Copper-grid) with a transparency of around 85% was glued on the outer surface along the entire length.

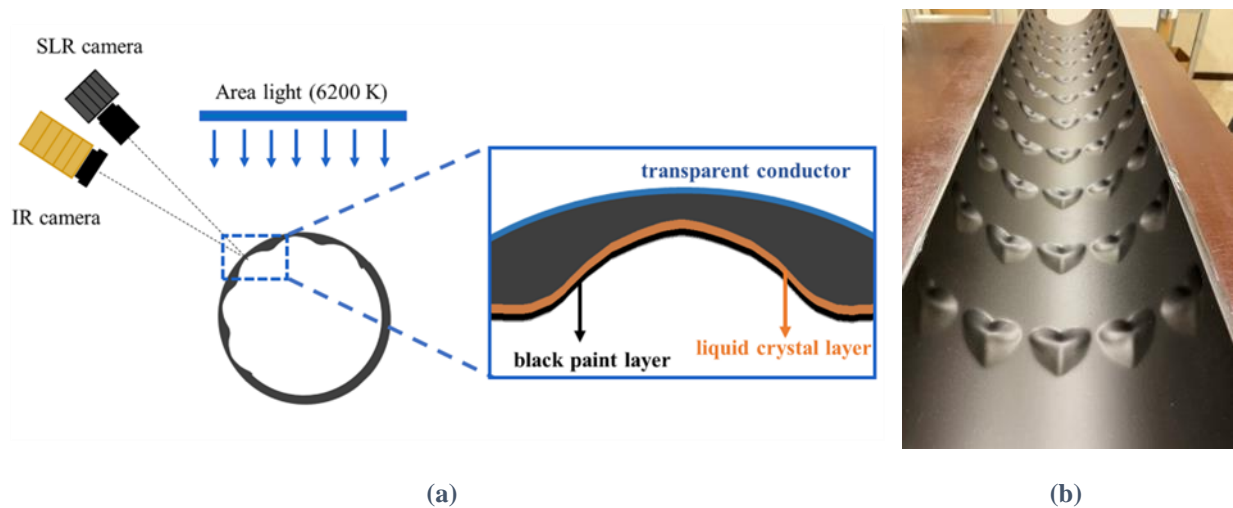


Figure 2: A side view illustration of the heat measurement configuration (a) including one dimpled half (b)

For the assessment of skin friction coefficient, two static pressure taps were installed at inlet and outlet of the dimpled pipe, enabling the measurement of the pressure drop across the entire pipe, i.e., the pressure difference between pipe's entrance and exit.

The calibration of the temperature measurements was done with great care. First of all, we calibrated three K-type thermocouples as references for the IR camera calibration and two K-type thermocouples for measuring the local flow temperatures at the inlet and outlet of the test section. A reference probe with a high-accuracy thermometer (ISOTECH TTI-10, $\pm 0.0012^\circ\text{C}$) was used in a liquid bath (ISOTECH Hyperion Basic) to measure the reference temperatures. An in-situ calibration of other devices was performed in the experimental facility with a particular configuration, as illustrated in Figure 3. The dimpled half was mounted to the pipeline with a 40° of rotation, ensuring consistency with the measurement configuration. The SLR camera was positioned about 1 meter away from the dimpled surface, at a 50° angle, such that the reflections caused by the light source could be minimized. The region of interest (ROI) in this study, presented in Figure 3, consists of the area with the dimensions of 80 mm in the streamwise direction and 24° ($\pm 1^\circ$) in the azimuthal direction, containing a heart-shaped dimple of the 9th row. The investigated dimple was taken as far away from the channel entry as possible to guarantee thermal development. The infrared (IR) camera was installed on the other side of the pipe, with its axis azimuthally aligned with that of the other SLR camera. Thus, the IR camera directly measured the temperature of the internal surface while SLR camera could record the colors scattered by the liquid crystals applied from the same field of view.

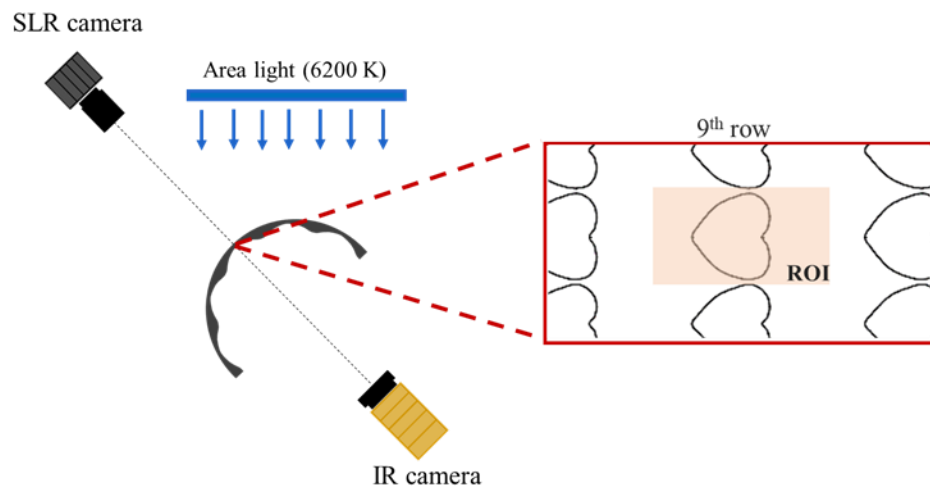
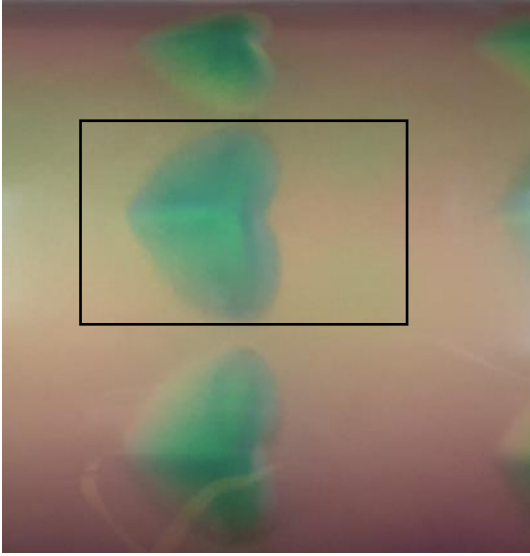
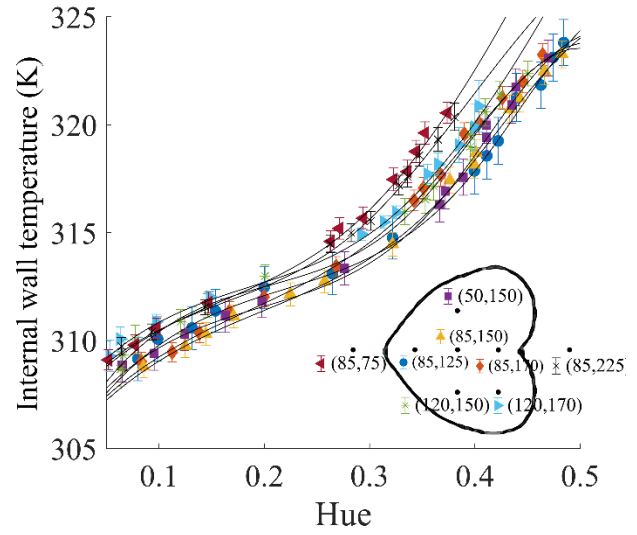


Figure 3: A side illustration of the configuration for heat transfer measurement calibrations together with the corresponding region of interest

An in-situ calibration, where the ambient temperature variations were neglected, was made for IR camera [14]. For the calibration function, to take the angular dependencies into account, the temperature values were taken from four thermocouples located at different positions in the ROI considering that the interested surface is highly curved [13]. The output signal of the IR camera was chosen as the raw intensity unit as it corresponds to raw pixel data without any correction applied for any parameter such as emissivity, relative humidity, distance, etc. A polynomial curve was fitted to a set of data points including all the calibration points. Like the IR camera in-situ calibration, **the thermochromic liquid crystals (TLCs)** were calibrated with all the camera parameters set to the measurement values. To obtain the required depth of field, the camera lens was set with a f/16 aperture. ISO sensitivity was selected to provide highly saturated colors and therefore minimum uncertainty in the investigation of TLC. The white balance was set to 6200K, the same color temperature value as the area light source. It was ensured that the IR camera records the same field of view (ROI) as the SLR camera. Both SLR and IR cameras recorded 15 different steady-state temperature field levels obtained within the operating temperature range of the liquid crystals (33-55°C) by adjusting the voltage values applied to the transparent conductor. Each pixel in the RGB images recorded with the SLR camera (one temperature field level is presented in Figure 4a) contains RGB (red-green-blue) intensities. These intensities were then converted into hue by utilizing the Hollingsworth equation [15]. In this case, hue values strongly depend on both temperature and coordinate because the complex surface of the dimple and the curved surface of the outer wall affect the colors digitally recorded by the camera. Therefore, each hue was individually matched with the corresponding pixel in the temperature field image recorded by IR the camera [10]. As a result, a particular cubic spline curve consisting of 15 calibration points was obtained for each pixel in the image as shown for several exemplary pixels in Figure 4b.



(a)



(b)

Figure 4: (a) An RGB image of a temperature field recorded level by SLR camera with the region of interest indicated; (b) Samples of the calibration curve fits at four random pixels

2.2.2 Data acquisition

The recordings of the measurements were taken at steady state condition for $Re=20k$, $30k$ and $55k$ flow regimes. Since the voltage required for higher Re numbers caused minor deformations on the gridded film, measurements at higher Reynolds were not possible. The energy required to sustain the steady condition comes from the heat generated by a DC voltage applied to the transparent conductor. The generated energy (\dot{q}_g) was then transferred through the pipe by means of heat conduction (\dot{q}_{cond}) as presented in Figure 5a.

However, a part of the generated energy is lost due to natural convection from the outer surface to the ambient and to radiation. Applying the conservation of energy to a control surface at the outer wall, the balance yields:

$$\dot{q}_g = \dot{q}_{cond} + \dot{q}_{nat,conv} + \dot{q}_{rad} \quad (1)$$

It is estimated that 12% of the total generated power is lost through natural convection [25] and 27% through radiation [26] to the test environment, with the remaining portion attributed to heat conduction. It is important to note that solving the natural convection ($\dot{q}_{nat,conv}$) and radiation (\dot{q}_{rad}) terms is beyond the scope of this study, and the primary focus lies on the conduction term which is determined through measured outer and internal wall temperatures. The energy carried to the

internal wall surface by heat conduction is then transferred to the airflow in the channel by means of forced convection. Consequently, the energy balance for a control surface on the internal wall takes the form:

$$\dot{q}_{cond} = \dot{q}_{conv} \quad (2)$$

Once the system reaches steady conditions, the IR camera and SLR camera record the same field of view for respectively the outer wall ($T_{w,out}(x, \theta)$) and the internal wall ($T_{w,int}(x, \theta)$) temperatures. Meanwhile, the air temperatures at the inlet and outlet of the test section were measured by K-type thermocouples located at the center of the pipe to define the bulk temperature (T_b). The heat transfer coefficient, h , for each element (pixels) in the ROI was calculated as:

$$h(x, \theta) = \frac{\dot{q}_{conv}(x, \theta)}{T_{w,int}(x, \theta) - T_b(x)} \quad (3)$$

where $q_{conv}(x, \theta)$ is the convective heat transfer from the internal wall to the air per unit area, and x , and θ are the axial and azimuthal coordinates. To determine T_b at different points along the axial direction, a linear interpolation was employed between the inlet and outlet temperatures. The convective heat transfer, $q_{conv}(x, \theta)$, was calculated by solving the 3D energy balance in both spherical coordinates (for the dimpled surface) and cylindrical coordinates (for the smooth surface) [10,16]. The radial component of heat conduction was calculated for each element with the linear temperature assumption through the pipe. Therefore, the component can be expressed as

$$\dot{q}_{cond,r} = -k_p \frac{T_{w,out}(x, \theta) - T_{w,int}(x, \theta)}{l(x, \theta)} \quad (4)$$

where l is the pipe thickness, k_p is the conductivity of the pipe. To minimize the uncertainties, the thickness of the pipe was obtained by scanning of the test section with an accuracy of +/- 0.01 mm and a resolution of 0.03mm. The thickness values based on x and θ are then matched with the pixel values to obtain the thickness map, $l(x, \theta)$, throughout the dimple (Figure 5b).

The Nusselt number is defined as:

$$Nu(x, \theta) = \frac{h(x, \theta)D}{k_{air}} \quad (5)$$

where k_{air} is the conductivity of the air at the film temperature and D is the inner pipe diameter. The comparison of the local Nusselt number over the dimpled ROI with that of the smooth tube was made through enhancement factor (EF), which is expressed as:

$$EF(x, \theta) = \frac{Nu(x, \theta)}{Nu_0} \quad (6)$$

where Nu_0 was estimated using the Dittus-Boelter correlation suggested for fully developed flows in circular channels:

$$Nu_0 = 0.023Re^{0.8}Pr^{0.4} \quad (7)$$

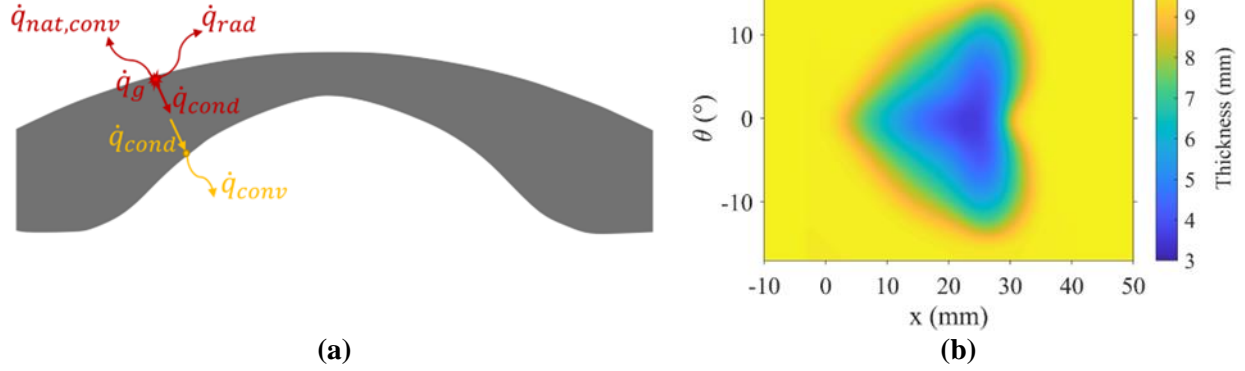


Figure 5: (a) A side illustration of the control surfaces on the dimpled wall; (b) Pipe thickness, $l(x, \theta)$, around investigated dimple provided by 3D scanning

The mean wall shear stress is found through the fact that the mean pressure gradient is balanced by the shear stress gradient and can be expressed as [27]:

$$\bar{\tau}_{wall} = -\frac{\Delta p D}{\Delta x 2}$$

where Δp is the pressure drop measured between the inlet and outlet of the pipe and Δx is the distance between measurement points. On the other hand, the skin friction coefficient is defined as the wall shear stress normalized by a reference velocity Based on the bulk velocity, U_b , in this study, it is calculated as:

$$C_f = \frac{\bar{\tau}_{wall}}{\rho U_b^2 / 2}$$

where ρ is the fluid density.

2.2.3 Uncertainty analysis

Although the TLC technique is widely used to determine surface temperatures, the results can be affected by several error sources such as hysteresis, illumination disturbance, angular dependencies, film thickness variations, image conversion systems, etc. [17,18]. These sources become even more critical when the technique involves multiple measurement chains affected by

a priori evaluated equations and numerous experimental parameters. In the current study, the temperature data was processed to determine the Nusselt number distribution across the complex dimpled surface. Measuring internal and outer wall temperatures for which four different calibrations were required: liquid crystals and IR camera at the internal wall, IR camera at the outer wall and the thermocouples. The uncertainty sources in the temperatures measured by current liquid crystal thermography consist of the conversion of RGB intensities into hue values, IR camera-induced errors, and the errors caused by fitted calibration curves. Meanwhile, the uncertainty in the IR camera measurements basically includes the fitting error between the IR camera signal and the measured temperatures, reading errors, thermocouple uncertainties, and the error that resulted from the fact that the object signal deviates around the value. This implies the need for a meticulous quantification of the uncertainty sources in the heat transfer coefficients, which has never been done for such dimple surfaces according to the authors' knowledge.

In this uncertainty analysis, the details of which are given in the appendix, a comprehensive examination of the uncertainties in the interior wall temperature, bulk temperature, outer wall temperature, pipe thickness, thermal conductivity of the pipe and air was conducted. The systematic ($b_{Nu,i}$) or random ($s_{Nu,i}$) uncertainties of each source are determined pixel by pixel (if required for pixel dependent parameters) in ROI. The sensitivities of Nusselt number to each source (S_i) were calculated to identify the uncertainty contributions and rank them in terms of their potential impact on the final uncertainty based on their measured values. Table 1 summarizes the outcomes consisting of the ranges of the measured quantities, systematic and random uncertainties, sensitivities, and contributions to the final relative uncertainty across the region of interest for each source. The mean values are included alongside the corresponding ranges. (For detailed results, please see Appendix A).

Pixel matching between the IR camera and SLR camera in TLC calibration resulted in lower random errors than systematic errors for the interior wall temperature. The sensitivity to the uncertainty in the pipe thickness is by far the largest compared to other sources. However, very low uncertainties in the thickness obtained by the high-accuracy scanning process contributed relatively less to the final value. That is the prior knowledge of the sensitivity in this study allowed us to take precautions to avoid higher uncertainties. On the other hand, in contrast, the interior wall temperature measured by the liquid crystals thermography contributed as one of the highest to the final uncertainty despite the lowest sensitivities. The biggest local contribution originated from the

temperature of the outer wall due to very low wall thickness of certain locations inside the dimple (about 0.3 times the wall thickness at smooth region).

Table 1: Summary of the uncertainty sources for the flow regime of $Re=20000$

	Value	$b_{Nu,i}$	$s_{Nu,i}$	S_i	$(b_{Nu,i}S_i)^2$	$(s_{Nu,i}S_i)^2$
$T_{w,int}$ [K]	34 - 46	0.25 - 0.91 (0.31)	0.13 - 0.86 (0.16)	0.45-11.04 (3.83)	0.75 - 6.60 (1.32)	0.05 - 7.82 (0.44)
T_b [K]	23.3	0.08	-	0.45-11.04 (3.83)	0.00-0.8 (0.1)	-
$T_{w,out}$ [K]	44 - 56	0.24	0.11	6.78-19.94 (8.42)	2.64-22.8 (4.08)	0.54-4.81 (0.85)
l [mm]	3.6 - 9.9	-	0.00	1304-23400 (6810.32)	-	0.00-0.23 (0.07)
k_p [W/mK]	0.228	-	0.00228	45.37-631 (275.43)	-	0.01-2.06 (0.39)
k_{air} [W/mK]	0.0235	0.000015	0.000258	404-5622 (2343.75)	0.00	0.01-2.10 (0.36)

Subsequently, the standard uncertainty on the Nusselt number was computed at a pixel-wise level by incorporating all relevant contributions through the combination of all terms. Figure 6 presents the overall uncertainties, defined at a confidence level of 95%, for the flow regime $Re=20k$ in both absolute and relative terms. Figure 6a shows the uncertainties as a numerical value, while Figure 6b presents the uncertainties as a percentage of the measured quantity. The downstream of the dimple exhibits the highest numerical uncertainty values due to the optical complexity of the dimple geometry around the trailing edge while the low heat transfer levels (as it will be discussed in the next section) inside the dimple lead to the highest uncertainty as a percentage relative to local Nusselt numbers.

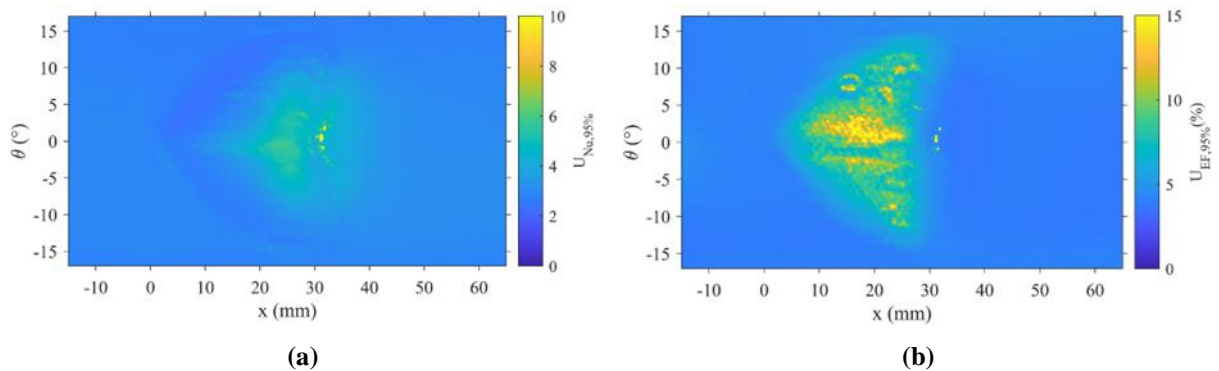


Figure 6: The expanded overall uncertainty field for the flow regime of $Re=20000$ around region of interest in Nu (a) and in percentage (b)

2.3 Flow field measurements

Advanced flow field measurements in the test geometry were conducted using PIV technique in another low-speed facility (Figure 7) designed to study the flow fields within circular channels. The detailed concept of the facility can be found in previous studies [10,13]. The test channel consisting of one smooth half and one dimpled half -the same as in the heat transfer facility- was installed in the test section. A rectangular transparent box enclosing the test channel ensured a flat interface between the ambient air and high refractive index medium before the curved surface of the channel. This box was filled with water to provide enhanced focus and refractive index matching, as well as to minimize optical distortions induced by the channel's surface.

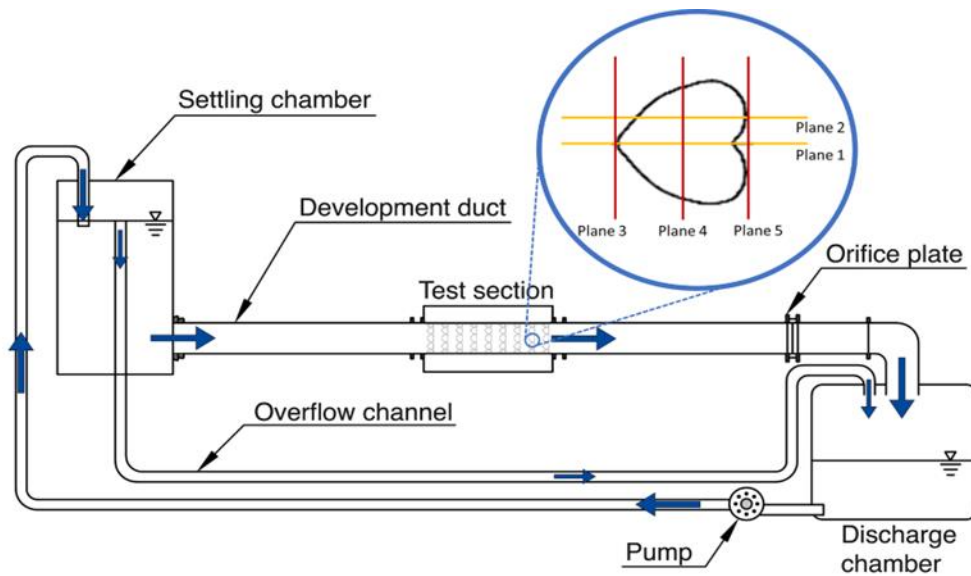


Figure 7: Experimental unit for Particle Image Velocimetry measurements of dimpled test section together with the measurement planes in both streamwise (Plane 1, 2) and spanwise (Plane 3, 4, 5) directions around the central dimple in 9th dimple row [13]

Both planar PIV and S-PIV measurements were carried out in the same position of the test channel: the acrylic smooth half at the top and the transparent heart-shaped dimpled half at the bottom. Five different measurement planes around the dimple investigated in the streamwise and spanwise directions at the flow regime of $Re=20k$ are illustrated in Figure 7. To ensure that the flow was sufficiently developed, the planes were located at the 9th dimple row as in the heat transfer investigation.

2D velocity fields in two planes in the streamwise direction were measured using planar PIV configuration (Figure 8). The measurement planes were located in the symmetry plane of the central dimple (Plane 1) and in the plane obtained by a pipe rotation of 7-degree (Plane 2), respectively. A dual frame CCD (Charge-Coupled Device) camera (Imager SX 4M) was

positioned in line with the ninth row, with its axis perpendicular to the box wall and parallel to the horizontal. Nikon AF-S 50mm f/1.8 NIKKOR lens was selected to receive a minimum amount of lens-induced image distortion. The optical accesses to both measurement planes were provided straight through the heart-shaped dimples which cause high-level image distortions due to their optically complex geometry. The measurement planes recorded in PIV images were calibrated using a 100x100 mm calibration plate made up of 2500 black dots with a 1 mm diameter. The calibration plate was placed so that it barely touched the central dimple's surface (Figure 8).

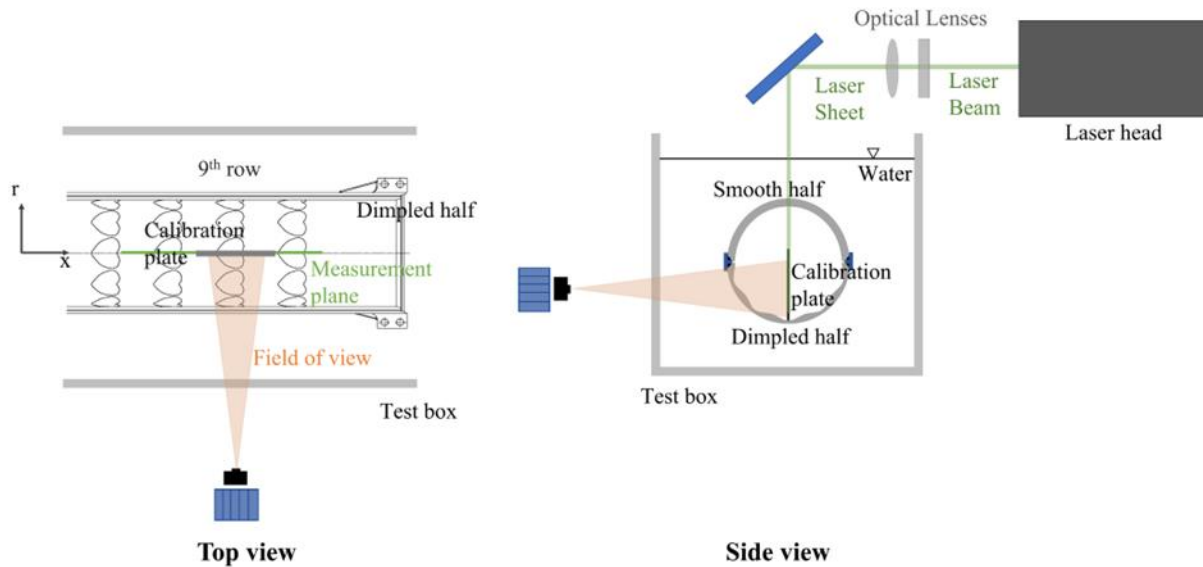


Figure 8: Planar PIV configuration

Figures 9a and 9c show the high level of distortions on the calibration images caused by the corresponding heart-shaped dimples. For accurate measurements of particle displacements during the vector calculations, the calibration images were reconstructed (Figure 9b and 9d) using an advanced ray tracing-based image correction method [11, 12] because the conventional approaches (3rd order polynomial, pinhole model, etc.) were insufficient for such distortions. Unlike the other approaches, instead of using a single mapping function for the entire image, this method provided a mapping matrix including pixel-by-pixel correspondences between the image plane and the measurement plane. It should be noted that the blank areas in the corrected images represent unrecoverable areas of the field of view although the corrections are made properly. That is because the blank areas are invisible in the raw calibration images as the rays coming are highly refracted by the heart-shaped dimple and therefore unable to reach the camera sensor. The standard deviations between the corrected images and references representing the ideal calibration

coordinates were calculated as 0.32 and 0.72 pixels for respectively Plane 1 and 2. However, although the RMS fit values were quite decent for PIV, the effect of the complex distortions on the accuracy of particle displacement measurement in both planes should be furtherly investigated. The mapping-induced uncertainties were therefore quantified via the synthetic particle image approach as proposed by Akkurt et. al [12]. In the analysis where 8 pixels of uniform particle displacements were applied, the maximum and average uncertainties were calculated as around 1% and 0.5% for Plane 1, respectively. Both results for Plane 2 were slightly reduced and were found as 1.1% and 0.5%.

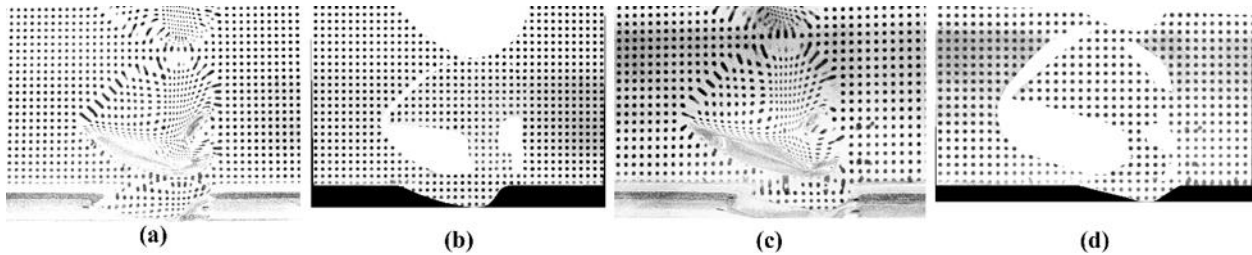


Figure 9: Recorded calibration images for Plane 1 (a) and Plane 2 (c) and their reconstructions by ray tracing-based image correction methods for respectively Plane 1 (b) and Plane 2 (d)

On the other hand, a stereoscopic PIV configuration (Figure 10), that was built in a similar concept as the study of Marco et al. [10], was employed to measure the three velocity components in three different planes in the spanwise direction: the upstream plane, the downstream plane, and the central plane. Two dual frame CCD camera (Imager SX 4M) equipped with the same 50mm NIKKOR lens were located with angles of $+45^\circ$ and -45° with respect to the measurement plane. Unlike the planar PIV cases, the cameras were slightly lifted to provide optical access to the measurement fields through the smooth half. In this configuration, water prisms were also used for both cameras to improve optical access and reduce perspective distortions. Additionally, scheimpflug adapters were also utilized to keep the image focused throughout the entire field of view in such an S-PIV configuration. For the calibration, a plate with a similar dot pattern was used. But the dots were printed on a transparent plate so that both cameras were able to detect the same dots on the plate. The plate was located perpendicular to the flow direction (Figure 10). In each S-PIV case, the calibrations were made by acquiring six images (three images by each camera) at three different parallel positions of the calibration plate with a 0.5mm in-between. Unlike planar PIV case, the calibration images were reconstructed by using 3rd-order polynomials in Davis 8.4.0 software - radially strong but regular distortions were experienced. The overall

standard deviations between the corrected images and references were obtained as 0.73, 1.07 and 0.89 pixels for respectively Plane 3, 4 and 5.

We illuminated all the measurement planes through the smooth half to avoid strong laser refractions caused by the complex dimple surface (Figure 9, 10). A dual cavity solid state Nd:YAG laser with maximum output energy of 200mJ and a wavelength of 532nm was used as laser source to generate the laser beam. The optical lenses were placed after the laser head to form a laser sheet with an average thickness of around 1.5mm. The laser sheet was then turned around 90° by a mirror (Gimbal mount – Edmund optics) towards smooth half and aligned with the measurement planes where the calibration plate is located. Fluorescent polyethylene seeding particles with 10-45µm were added in the flow to scatter both the wavelength of the laser (523 nm) and emit a larger wavelength. The light with the laser wavelength was blocked using a notch filter (Techspec OD 6.0), leaving the camera sensor to receive the light re-emitted by the particles. To obtain PIV images free of background noise, light reflections from undesired sources such as reflective surfaces and air bubbles formed in water were prevented. For each measurement case, PIV raw images were recorded using Davis 8.4. 1000 image pairs were acquired at a frequency of 1 Hz with the camera's f-number set to 5.6. To guarantee that the maximum particle displacements would be about 8 pixels, the separation time between two successive PIV images were individually determined for each experiment.

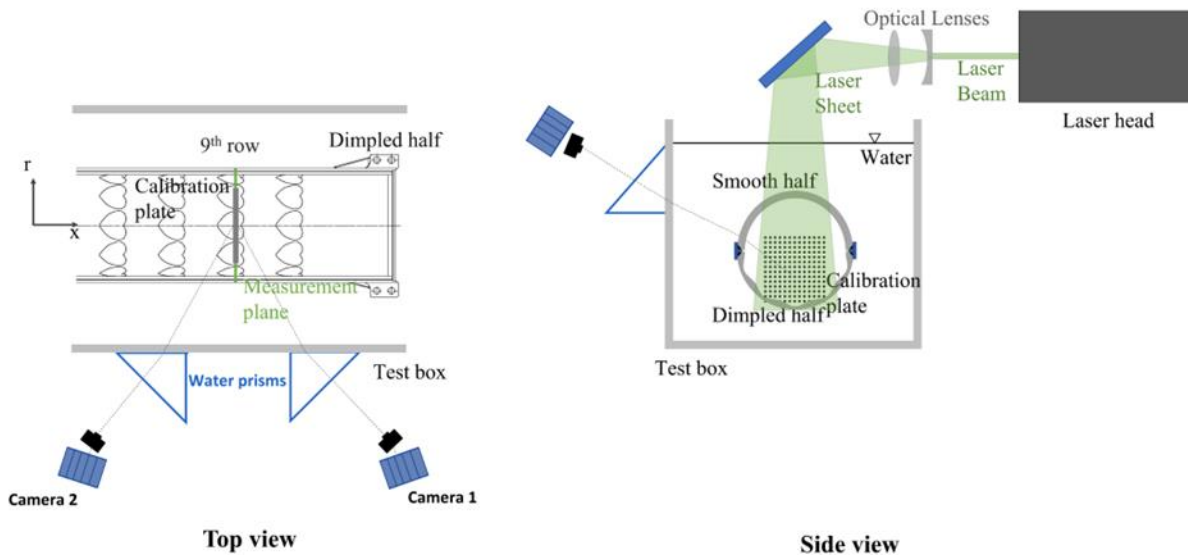


Figure 10: Stereoscopic PIV configuration

After the acquisitions, the background images generated separately for each case by a **POD (Proper Orthogonal Decomposition) based method**, which is proposed by Miguel et al [19], were removed from the raw PIV images before the image corrections. Instantaneous velocity fields were calculated in Davis 8.4 by the cross-correlation algorithm of the software run with the final interrogation windows of $32 \times 32 \text{ pix}^2$ in three refinement steps. During processing, a 50% effective interrogation window overlap was used. The parameters such as the measurement distance, focal length, camera sensor size, interrogation window size and the overlap resulted in the final spatial resolutions of approximately $1 \times 1 \text{ mm}^2$ and $1.4 \times 1.4 \text{ mm}^2$ for planar and stereo PIV configurations, respectively. The mean ensembled uncertainties were calculated via the method by Sciacchitano et al. [20] in the software. Table 2 shows the uncertainty values of the three velocity components (or two components in Plane 1) in percentage. In Plane 2, the maximum values are located inside the dimple and in the low-velocity region, whilst the regions subjected to high distortions due to the dimples caused the most significant uncertainties in Plane 1.

Table 2: The overall uncertainties of the velocity components in PIV measurements

Measurement plane	$\mathbf{u}_{\theta,max}$	$\mathbf{u}_{\theta,avg}$	$\mathbf{u}_{r,max}$	$\mathbf{u}_{r,avg}$	$\mathbf{u}_{x,max}$	$\mathbf{u}_{x,avg}$	\mathbf{U}_{max}	$\mathbf{U}_{max,avg}$
Plane 1 (2D)	-	-	5.8%	0.91%	4.1%	0.7%	4.2%	0.7%
Plane 2 (2D)	-	-	6.1%	0.92%	4.9%	0.8%	4.9%	0.8%
Plane 3	4.4%	1.3%	10.6%	2.0%	2.7%	1.2%	2.8%	1.2%
Plane 4	4.8%	1.7%	11.9%	2.6%	2.5%	1.1%	2.6%	1.2%
Plane 5	3.3%	1.6%	9.2%	2.2%	2.4%	1.3%	2.4%	1.3%

3 Results

The flow field of the central dimple at the 9th row was investigated in two planes in the streamwise direction and three planes in the spanwise direction using respectively planar PIV and stereo-PIV measurements. The 2-D time-averaged axial and radial velocity field contours in the streamwise planes (Plane 1 and 2) are illustrated together with the mean streamlines in Figure 11. The blank areas in the contours indicate the invisible areas in both measurement planes due to lack of optical access and they were excluded from PIV calculations. In the plots, the y-axis represents the radial positions where $r/R=0$ and $r/R=1$ correspond respectively to the center and the wall of the circular

channel. The axial location $x=0\text{mm}$ coincides with the dimple's leading edge in the symmetry plane where the flow separation starts. This flow separation generates localized regions of low pressure and, as the streamlines illustrate in Plane 1, a recirculation vortex is formed in the dimple by the impingement of the upstream flow directly to the back rim of the dimple, which are leading to pressure loss and local heat transfer deterioration. The center of the recirculation bubble is situated within the downstream half of the dimple and located at $x=21\text{ mm}$ near the trailing edge. This position is also clarified by the distribution of the radial velocities inside the dimple (Figure 11b). The negative components are gathered in the rear part of the downstream half while a wider positive radial velocity zone takes place towards the leading edge. A narrow zone with almost zero radial velocity appears in-between. The presence of strong radial velocity components at the downstream edge of the dimple represents the upwash zone, where the flow is pushed out of the dimple and mixed with the core flow. The reverse flow region is characterized by the negative values of the axial velocity and extends all the way to the separation point at the leading edge.

Figure 11c and 11d show that the leading edge in Plane 2 is located slightly downstream, $x=7\text{mm}$ due to the tapered shape of the front edge. The axial velocity profile above the low-pressure zone inside the indentation is strongly similar to that of the symmetry plane. In both cases, the streamlines are parallel to the wall and the core flow is not affected by the dimple when $r/R < 0.9$. Due to the characteristic broader trailing edge of the heart-shaped dimple, another recirculation bubble is captured also in Plane 2. Due to the mild levels of radial velocities inside the dimple, the structure of the vortex is smaller than in Plane 1 and the center of the recirculation bubble is located slightly ahead. The upwash zone at the trailing edge is represented by the accumulation of the high positive components of the radial velocities in Figure 11d.

Figure 12 shows streamlines in the dimples plotted on the vorticity fields in Plane 1 and 2. Due to two-dimensional flow fields in both planes, the vorticity, ω , in the z -direction is calculated as follows:

$$\omega = \frac{1}{2} \left(\frac{\partial v}{\partial x} - \frac{\partial u}{\partial y} \right) \quad (8)$$

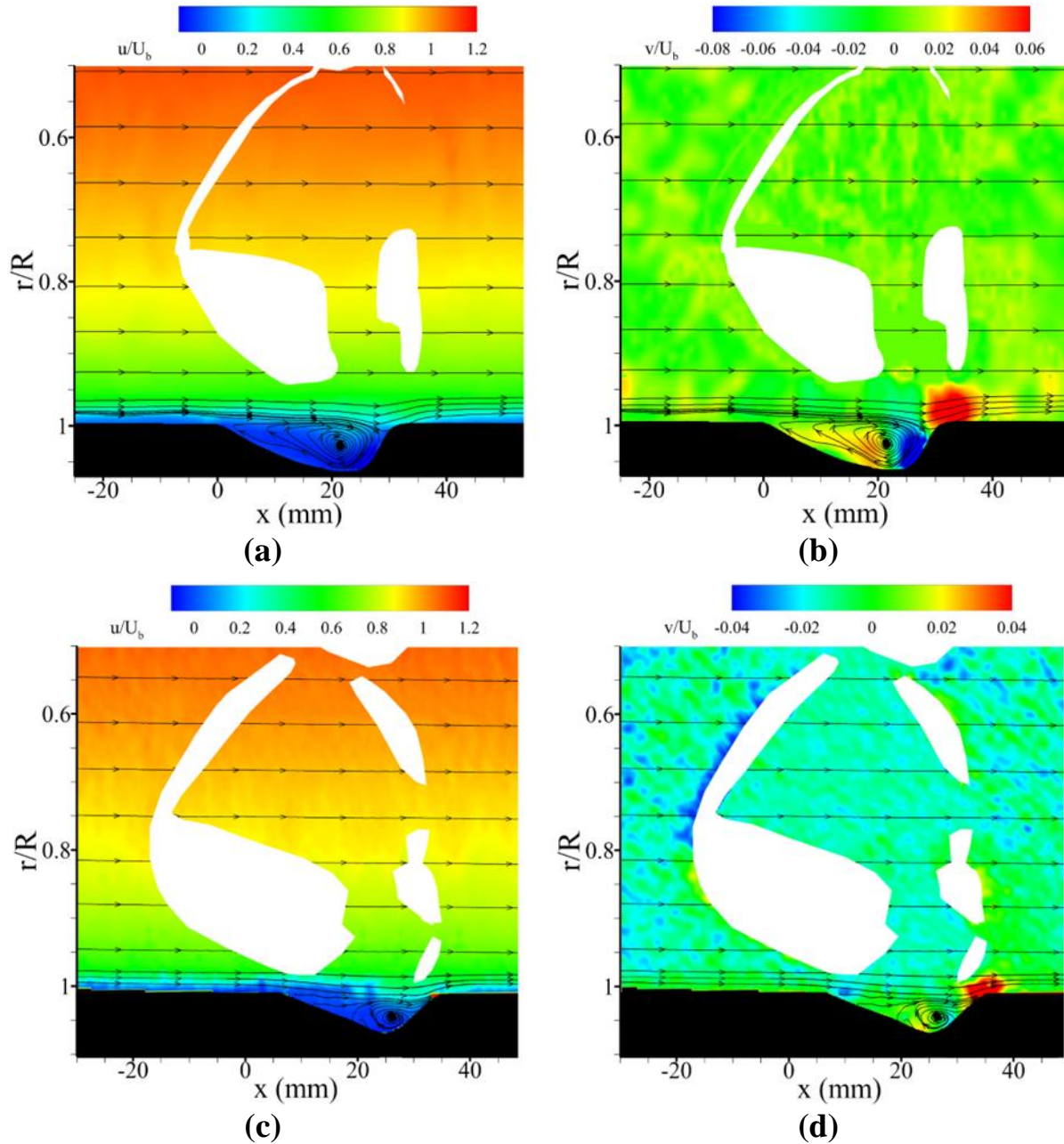


Figure 11: 2D velocity fields at $Re = 20000$: (a) axial velocity field in Plane 1 (symmetry plane), (b) radial velocity field in Plane 1 (symmetry plane), (c) axial velocity field in Plane 2, (d) radial velocity field in Plane 2

Although both vortices rotate in the clockwise direction, the structure in the symmetry plane circulates towards the center while in Plane 2 the recirculation occurs from the center outwards. This means that the symmetry plane vortex develops sideways inside the dimple and is swept towards downstream by the flow above before it is pushed out of the dimple at the trailing edge. This is in an agreement with the flow structures obtained by Dedeyne et al. [2]. Additionally, this vortex interacts with the main flow moving towards the leading edge, resulting in the flow

separation at around $x=0$ in Figure 12a. The separation point takes place relatively downstream on Plane 2 due to the position of its leading edge. The reverse pressure gradients caused by the flow separation die out before the downstream edge of the dimple with the help of the flow above the vortex, forming the reattachment points. In Plane 1, the flow reattaches to the wall just downstream of the dimple at around $x=29\text{mm}$ while the reattachment point in Plane 2 is slightly shifted into the dimple's back rim and is at around $x=33\text{mm}$. In both vorticity fields, the positive values of the vorticity are mostly concentrated in the shear layer. The positive vorticities develop between the wall and the recirculation bubbles, representing the formation of secondary structures contributing to the heat removal from the wall.

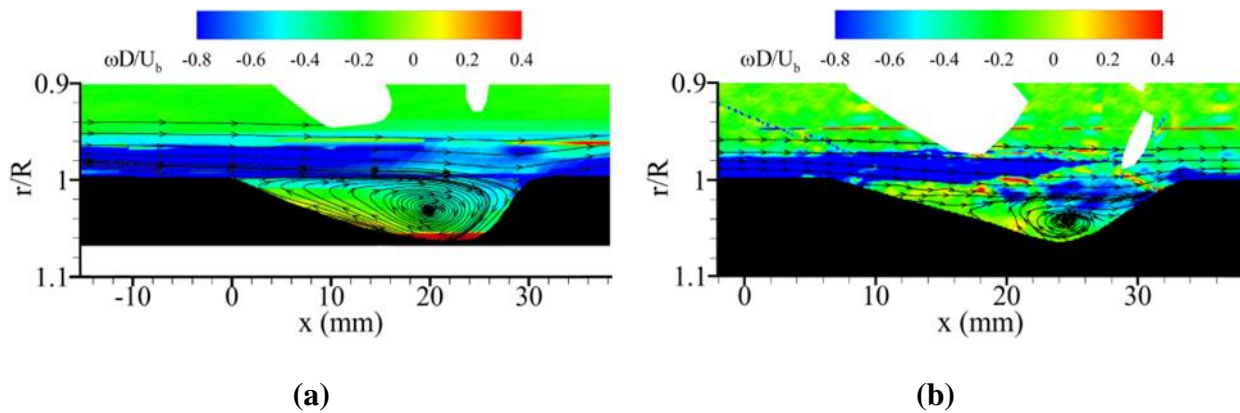


Figure 12: 2D vorticity fields at $Re = 20000$ in Plane 1 (a) and Plane 2 (b)

The fields of the three velocity components -axial, radial and azimuthal velocity- obtained from S-PIV in the middle plane and the downstream plane in the spanwise direction (Plane 4 and 5) are presented in polar coordinates in Figure 13. The x-axis of the plots represents the angular coordinates in degrees where 0° corresponds to the symmetry plane. Similar to the streamwise plane results, the y-axis corresponds to the radial coordinates nondimensionalized by the radius of the tube, r/R . In the mid-plane, velocities towards opposite side edges are seen in the low-pressure region inside the dimple (Figure 13a). These velocity zones represent the movement of the two separate vortices shed from the axial centerline of the indentation. The radial velocity field in the same plane (Figure 13b) reveal mild upwashing zones at the side edges, where the fluid is pushed towards the center of the tube.

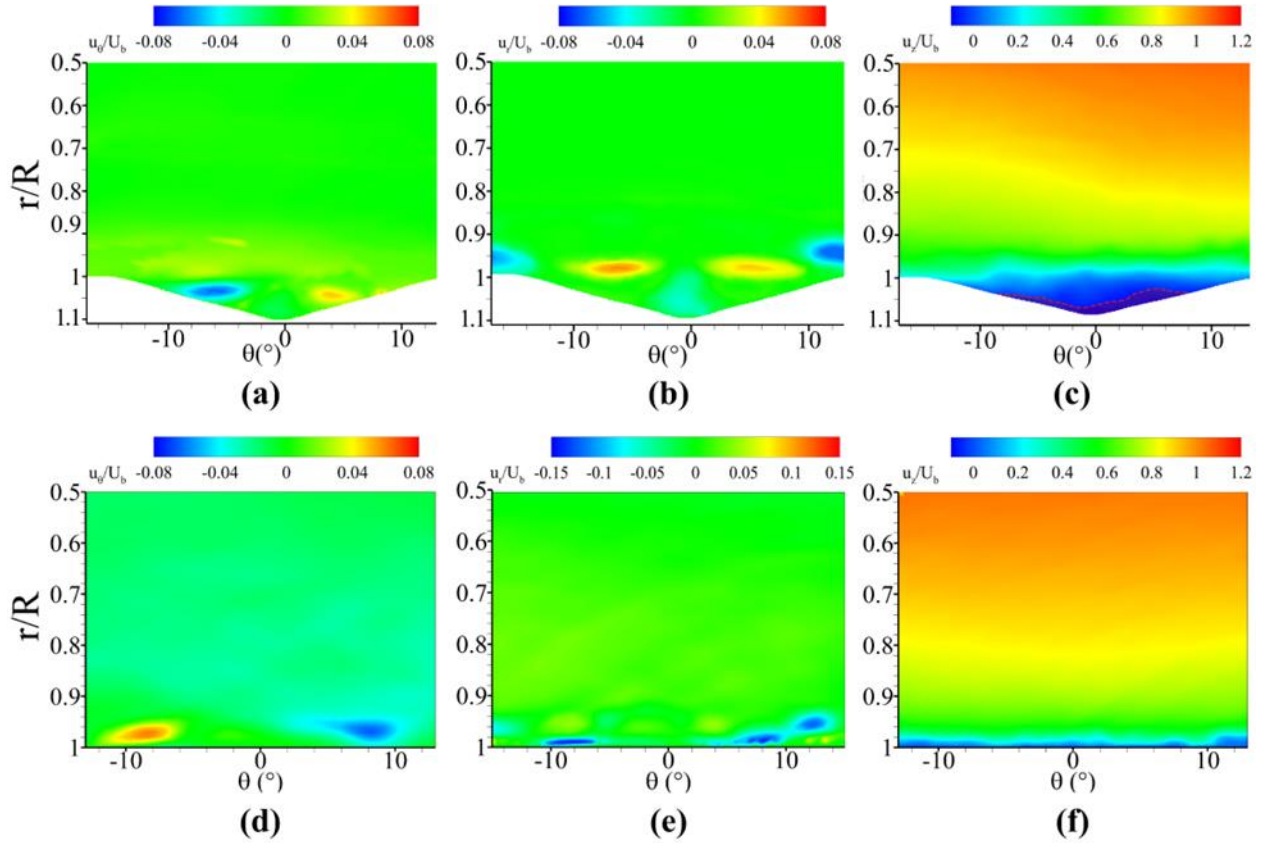


Figure 13: 3D velocity fields by S-PIV at $Re=20000$: (a) azimuthal velocity field in Plane 4, (b) radial velocity field in Plane 4, (c) axial velocity field in Plane 4, (d) azimuthal velocity field in Plane 5, (e) radial velocity field in Plane 5 and (f) axial velocity field in Plane 5

The counterflow region is separated from the positive axial velocities by the zero-velocity line (red dashed line in Figure 13c) close to the wall inside the dimple. The azimuthal and radial velocity fields in the downstream plane (Figure 13d, e) illustrate that the low-speed vortices laterally shed from the centerline are thrown out from the symmetrical lobes of the dimple. Reversely signed velocity zones in the azimuthal velocity field indicate that the flow here is headed in opposite directions, creating mild shedding.

Figure 14 shows the EF spatial distribution across the interested region of the heart-shaped dimple that is located at the center in the 9th row (Section 2) at the flow regime of $Re=20k$. The y-axis is the angular position in degrees, with 0 degree being the axis of symmetry. The x-axis represents the axial position in mm and includes the whole dimple row. At the leading edge of the dimple, the separation region results in the EF values lower than unity, which means that the heat transfer rates are lower than that of smooth pipe. The reference Nusselt number Nu_0 for the smooth pipe was calculated as 54 by the Dittus-Boelter correlation. The recirculation vortex, caused by the low-

pressure zone at the front of the dimple and the high-pressure zone resulting from the impingement of high-pressure flow at the rear edge of the dimple, extends towards the leading edge. Consequently, EF ratios remain below 1 in the throughout the recirculation zone upstream part. These findings are in alignment with the previous experimental studies where PIV and LCT are combined [10, 24]. In this zone, the minimum value calculated as 0.68. As the flow is moving downstream in the dimple, EF rises above 1. The highest local heat transfer enhancements occur at the trailing edge, where the boundary layer reattaches to the wall. The maximum is found around the symmetry plane of the shape ($\theta = 0$), equal to 2.7. Behind the dimple, due to the thin boundary layer thickness, EF values are still above 1 and lie within the range of 1.5-2.7.

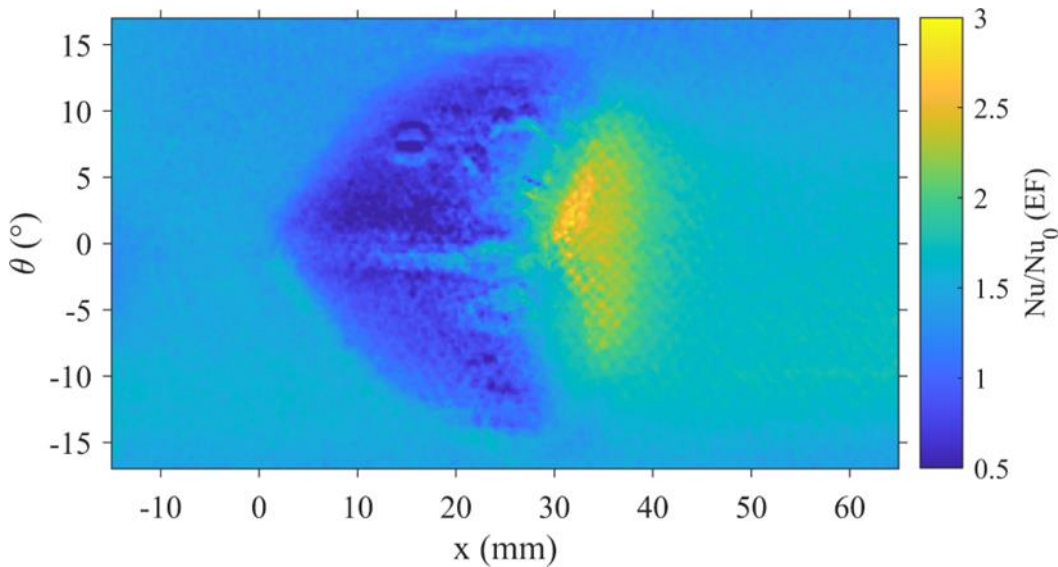


Figure 14: Enhancement factor field around the dimple in the region of interest at the flow regime of $Re=20000$

To confirm the heat transfer field periodicity, the results were compared with the dimple just upstream through the enhancement factor distributions. Detailed EF distributions along the azimuthal and axial planes for both 8th and 9th dimple surfaces are presented in Figure 15. The figures show that the heat transfer behaviours are quite similar in both dimples. All axis positions in Figure 15a support that Nusselt number distributions are symmetric with respect to the plane of symmetry ($\theta = 0^\circ$). It is shown that the enhancement factors are slightly lower for 9th the row in the regions corresponding to the inside of the dimples where the uncertainties in the enhancement factor are the highest. Similarly, it is observed that the values calculated along the axial direction (Figure 15b) slightly deviates from each other, especially inside the dimple region. But the heat

transfers from both dimples are mostly compatible (with a %1.9 deviation of overall value) with each other having the confidence levels overlapped almost all over the region of interest.

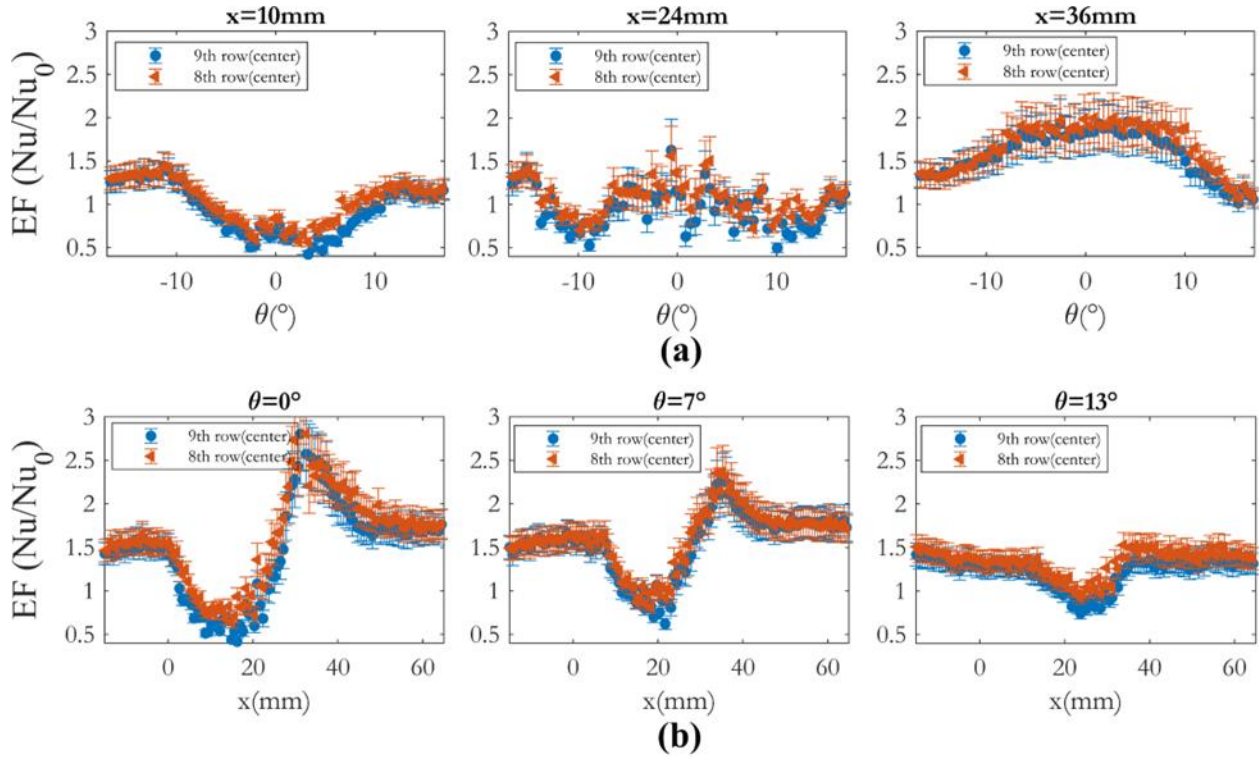


Figure 15: Enhancement factor distributions for the dimples at 8th and 9th rows along the azimuthal (a) and the axial (b) directions

The effect of Reynolds number on the heat transfer from the dimpled surface was investigated throughout the flow regimes of $Re=20k$, $30k$ and $55k$. EF distributions along the axial direction at different angles are presented in Figure 16a. Although all distributions substantially overlap, the flow regime, $Re=20k$, provides slightly lower heat transfer rates for the majority of the planes. The EF range of the asymmetric distributions that took place along the axial positions gets narrower as the angular position increases, i. e., as it moves away from the center. All the distributions have plateaus downstream and upstream of the dimple. Compared to other planes, in the symmetry plane ($\theta = 0^\circ$), the difference between the heat transfer values in the downstream region and the upstream region of the dimple is considerably large (around 1.8 downstream, 1.5 upstream). As illustrated in Figure 16b, each axial position provides similar EF profiles along the azimuthal direction. $Re=20k$ has slightly lower heat transfer rates compared with the others as it does in the previous comparison above. Especially, the deviation of the EF profile is most prominent at $x=0$ in the region $\theta = -10^\circ + 10^\circ$. For all profiles except $x=8mm$, the maximum values are located in the

center. On contrary, at $x=8\text{mm}$, the minimum levels of EF are accumulated around the symmetry plane because the flow is separated near the leading edge in a very narrow span.

Figure 17 illustrates the nondimensionalized turbulent kinetic energy fields and enhancement factor evolution across the streamwise and spanwise planes to indicate the correlation between turbulent mixing levels and heat transfer enhancements in the turbulent flow. In the s-PIV cases where three components of the velocity vectors are computed, the turbulent kinetic energy (TKE) quantity is defined as:

$$TKE = \frac{1}{2} [(u - \bar{u})^2 + (v - \bar{v})^2 + (w - \bar{w})^2] \quad (9)$$

For the planar PIV cases, because two velocity components were retrieved (in the streamwise planes), “in plane” TKE is instead introduced as:

$$TKE = \frac{3}{4} [(u - \bar{u})^2 + (v - \bar{v})^2] \quad (10)$$

where the third component of the velocity, w , is considered to exhibit similar turbulent contribution to the measured components, u and v , which are provided by the planar PIV. TKE fields in both streamwise planes (Plane 1&2) show EF decreases from the flow separation zone, responsible for the heat transfer deterioration, until the positions where the turbulent kinetic energy has the minimum levels inside the dimple. After reaching the lowest values, EF rises due to an increase in TKE in the separated shear layer. Higher enhancement factors are located around the flow attachment and upwashing regions in the downstream of the dimple, while the maximum is found at $x=32\text{mm}$ in the axial centerline (Figure 17a). The correlation between TKE and EF is supported by the highest values of turbulent kinetic energy around this location (around 5% of bulk kinetic energy). In Plane 2, the highest value moves a bit downstream and the reattachment point occurs earlier relative to the back rim of the dimple.

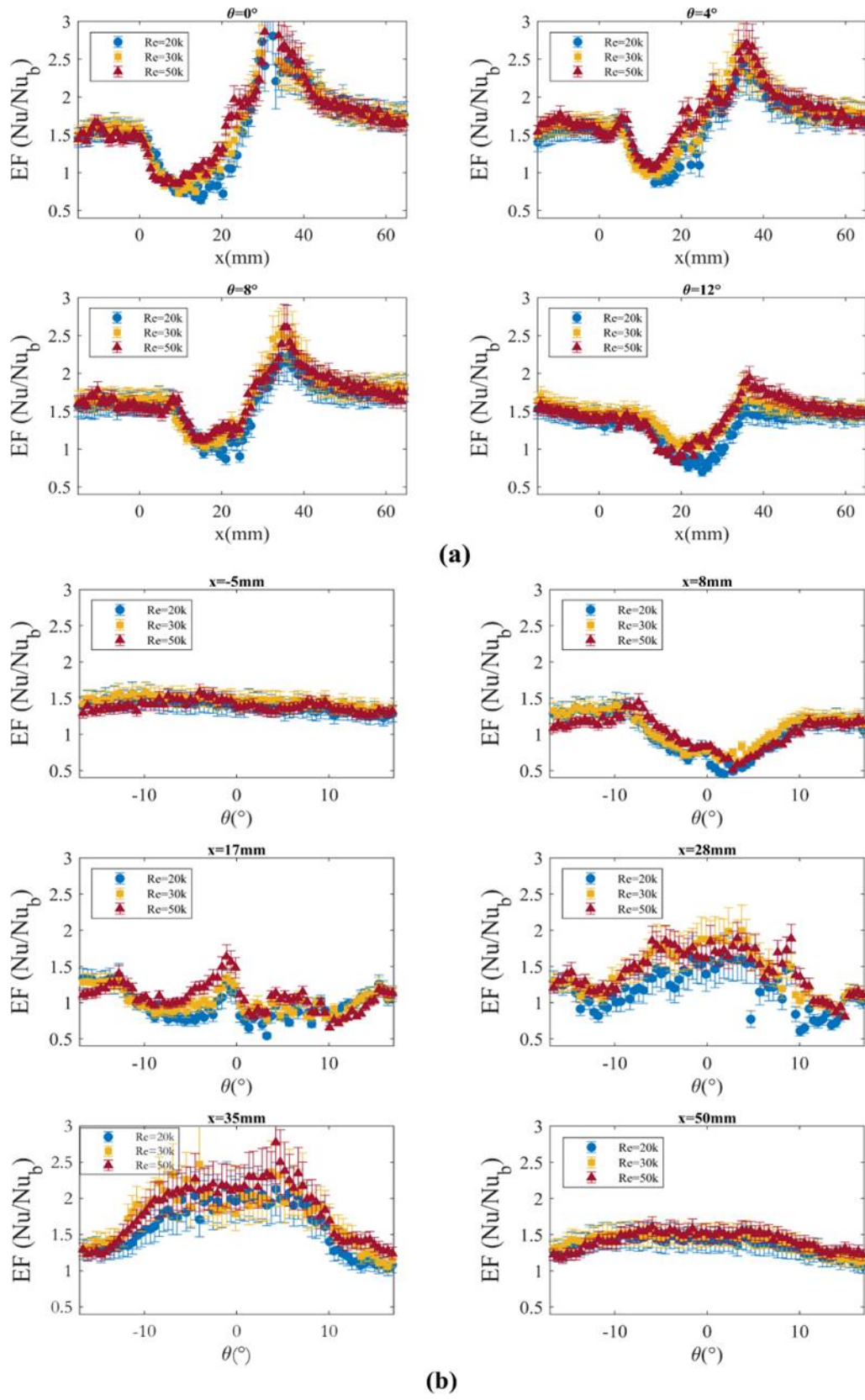


Figure 16: Enhancement factor distributions for the dimples at flow regimes of $Re=20k$, $30k$, $50k$ along the axial (a) and the azimuthal (b) directions

Around the upwashing region, where the downstream plane is investigated (Figure 17e), flow produces high turbulent mixing between the main flow with high speed and the low-speed flow inside the dimple, resulting in higher convective heat transfer coefficients [1,3,7]. Due to the shear layer, high TKE values upstream and downstream are bounded close to the wall. But TKE values are higher at the downstream as the boundary layer is developing after the reattachment line. Therefore, the EF plateau before the separation has slightly lower values (around 1.5) than the EF after the reattachment point. In the midplane (Figure 17d), the higher values of turbulence are accumulated in the central part, increasing the momentum transfer between the free flow with high momentum and the flow with low momentum in this region, also leading a local maximum of EF around $\theta=0^\circ$.

The skin friction coefficients in the heart-shaped dimpled tube in the range of Re number=20k-60k are presented in Figure 18a along with those of two different ribbed tubes [16] and a tube with spherical dimples [13]. Dimpled tubes have significantly lower skin friction coefficients than the ribbed tubes while heart-shaped dimples cause slightly lower frictions compared to the spherical dimples. No significant effect of the Re number on the coefficient is observed as in the other geometries.

The chart in Figure 18b shows EF values with the corresponding nondimensionalized skin friction coefficients (the value from the smooth pipe) for the overall performance comparison. The heart shaped dimpled pipe causes slightly lower skin friction coefficients compared to spherical dimples yielding less pressure drops. For corresponding configurations spherical dimples provide better heat transfer enhancement in terms of averaged EF in the related region of interest. It should be noted that the uncertainty included values overlap within the ranges of the two measured quantities. On the other hand, heart shaped dimples provide at least as much heat transfer enhancement as the ribbed tubes despite reduced pressure penalties.

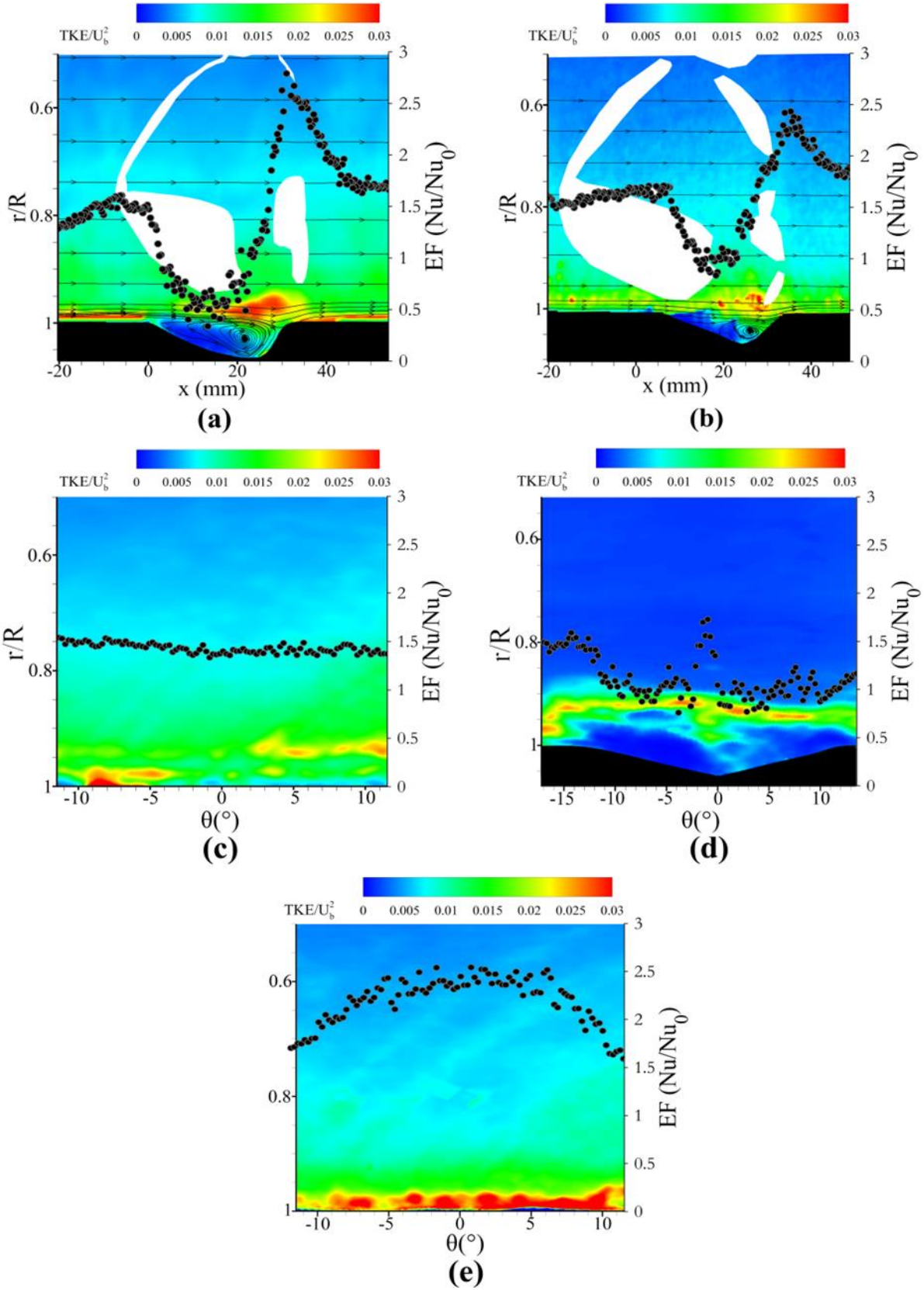


Figure 17: Turbulent kinetic energy fields in five measurement planes: (a) Plane 1 (b) Plane 2, (c) Plane 3, (d) Plane 4, (e) Plane 5

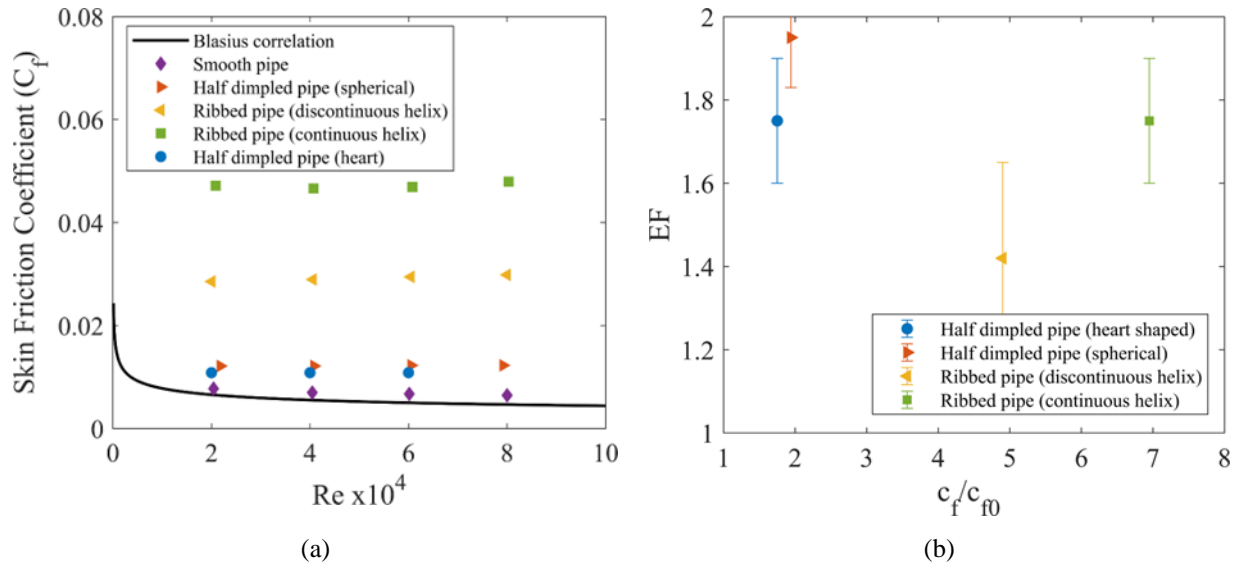


Figure 18: (a) Variation of the skin friction coefficients depending on the Reynolds number for different roughness elements employed in pipes; (b) Aero-thermal comparisons of the roughness elements

4 Conclusions

The flow structures and the heat transfer phenomena around a heart shaped dimple were measured to fully capture the heat transfer enhancement in a complex heart shaped dimpled pipe. The flow structures were investigated at a flow regime of $Re=20k$ using planar PIV and S-PIV configurations in five different measurement planes in respectively streamwise and spanwise direction. Despite the optically complex shape yielding severe irregular image distortions our ray tracing method decreased the possible calibration fit errors by means of the pixelwise correction algorithm (around 0.4 and 0.6 pixels for respectively Plane 1 and Plane 2). The convective heat transfer around the same dimple was measured by means of liquid crystals in the range $Re=20k-60k$ in a second facility.

The investigation showed that the vortex formed inside the dimple is positioned towards its downstream part due to the heart shape. The asymmetrical vortex structure leading to heat transfer enhancement is more localized around the downstream unlike the spherical dimples. The vortex at the symmetry plane is developed laterally and pushed out from both lobes of the dimple. The heat transfer rates are the highest where the flow reattaches to the wall in the downstream portion of the dimple. The enhancement factor decreased with separation at the dimple leading edge and reached its lowest value in the recirculation zone where the turbulent kinetic energy is the

minimum. As the TKE increased towards the downstream, the EF augmented yielding the maximum around the reattachment point. The improvement effect of the dimple stretches out at least to the successive dimple as the enhancement factor never reached unity until the next separation point although it kept getting lower as the TKE decreases and the flow develops. On the other hand, the flow regime had a slight influence on the heat transfer enhancement profiles. The general trend of the profiles was quite similar, but for Re=20k it resulted in a lower heat transfer, especially around the dimple centre. ROI averaged enhancement factors varied from 1.6-1.8 depending on the Re number. The pressure drop measurements illustrated that in comparison with a spherical dimpled channel and two different ribbed channels that heart shaped dimples result in the lowest skin friction. This proves that the optimized dimple shape an attractive solution particularly for the applications where the low-pressure penalties are aimed.

Appendix: Uncertainty analysis for Nu

Uncertainties are classified as systematic or random uncertainties based on whether they are caused by systematic or random error sources. Random errors are due to irregular factors affecting a measurement, so they can typically yield fluctuant values throughout a series of measurements and their mean value is expected to be zero. However, unlike random errors, systematic errors are constant and can be removed from the total error when their magnitude and sign are known [21]. In this case, the combined standard uncertainty in the quantity of measured Nusselt number is expressed as the sum of squares of the systematic, b_{Nu} , and random uncertainties, s_{Nu} [18]:

$$u_{Nu} = \sqrt{b_{Nu}^2 + s_{Nu}^2} \quad (11)$$

By the definition of the combined standard uncertainty, the probability of the total error falling within the range of $\pm u_{Nu}$ cannot be calculated. Therefore, an expanded uncertainty is considered with a confidence level:

$$U_{Nu} = k u_{Nu} \quad (12)$$

where k is the coverage factor and its values 1, 2 and 3 correspond to confidence intervals of 68%, 95% and 99.7% respectively.

Since several measurements are made and multiple terms are used to calculate the Nusselt number field, each uncertainty source needs to be accurately identified. Each source of measured quantities

contributes to the uncertainty according to the corresponding sensitivity (S_i) of the Nusselt number. The sensitivities are required to identify and rank the sources in terms of their potential impact on the final uncertainty based on their measured values. The overall systematic and random uncertainties associated with Nu are then expressed as:

$$b_{Nu} = \sqrt{\sum_i (S_i b_{Nu,i})^2} \quad (13)$$

$$s_{Nu} = \sqrt{\sum_i (S_i s_{Nu,i})^2} \quad (14)$$

In the present study, the sensitivities to uncertainties of each source included in the sum of the overall terms are analyzed scrupulously and pixel-wise, as they vary across the field of view. Following that, all the uncertainty terms are combined to define the standard uncertainty on the Nu number calculated pixel-by-pixel due to pixel-dependent parameters such as the internal and outer wall temperatures. The overall uncertainty on Nu number defined at a confidence level of 95% is expressed as suggested by ASME PTC 19.1-2005 [22] as:

$$U_{Nu,95}(x, \theta) = 2u_{Nu}(x, \theta) \quad (15)$$

1. Internal wall temperature uncertainty

As the internal wall temperature is measured by liquid crystals thermography, the errors occurred during the conversion of the RGB intensities of each pixel in the image recorded by the SLR camera into the hue values need to be considered. Quantization errors for RGB values are expressed taking into account 8-bit resolution of the camera as:

$$b_R = b_G = b_B = \frac{255/2^{8+1}}{\sqrt{3}} \quad (16)$$

Therefore, the digital camera resolution-induced systematic uncertainty can be calculated via

$$b_{T,RGB} = \sqrt{\left(\frac{\partial H}{\partial R} b_R\right)^2 + \left(\frac{\partial H}{\partial G} b_G\right)^2 + \left(\frac{\partial H}{\partial B} b_B\right)^2} \frac{\partial T}{\partial H} \quad (17)$$

where R, G, B are respectively red, green, blue intensities and H is the hue value defined by the Hollingsworth equation [15]. It should be noted that as each pixel in the region of interest is investigated separately due to the previously mentioned dependencies, the error caused by the temperature-dependent hue value in each pixel is independently considered. Similarly, the

derivative $\partial T/\partial H$ is computed through the spline curve fit obtained for the corresponding pixel element.

Moreover, the IR camera-induced uncertainties contribute to the internal wall temperature uncertainty since hue values are calibrated with the temperatures recorded by IR Camera. This error basically includes the fitting error between the IR camera signal and the measured temperatures, reading errors, thermocouple uncertainties and the error that resulted from the fact that the object signal deviates around the value. For the overall wall temperature measurement by the IR camera, the systematic and random uncertainties are calculated to be 0.25 K and 0.13 K, respectively. Finally, the spline curves fitted to the data points of 15 calibration levels to obtain the internal wall temperature values yield pixel-wise random errors which can be estimated as:

$$s_{T_{w,int,fit}}(x, \theta) = \sqrt{\frac{1}{v} \sum_1^N (T_{w,int,fit}(x, \theta) - T_{w,int,IR}(x, \theta))^2} \quad (18)$$

where v is the degree of freedom defined as the number of points data points (N) minus the number of knots in the curve fit plus 4 [18].

The expanded uncertainties in the internal wall temperature measured at the ROI under the steady state condition in the flow regime $Re=20k$ are presented in Figure 19. The maximum levels are located at the trailing edge of the dimple in the symmetry plane, where the deepest point of the dimple is skewed downstream. This is mainly due to the curve fitting errors of the hue values around this complex region as the sharp angle changes make the color observation optically challenging.

To express the propagation of the uncertainties in the internal wall temperature into the result of Nusselt number, the sensitivity is calculated by the partial derivatives as:

$$S_{T_{w,int}} = \frac{\partial Nu}{\partial T_{w,int}} = \frac{\partial Nu}{\partial h} \frac{\partial h}{\partial T_{w,int}} \quad (19)$$

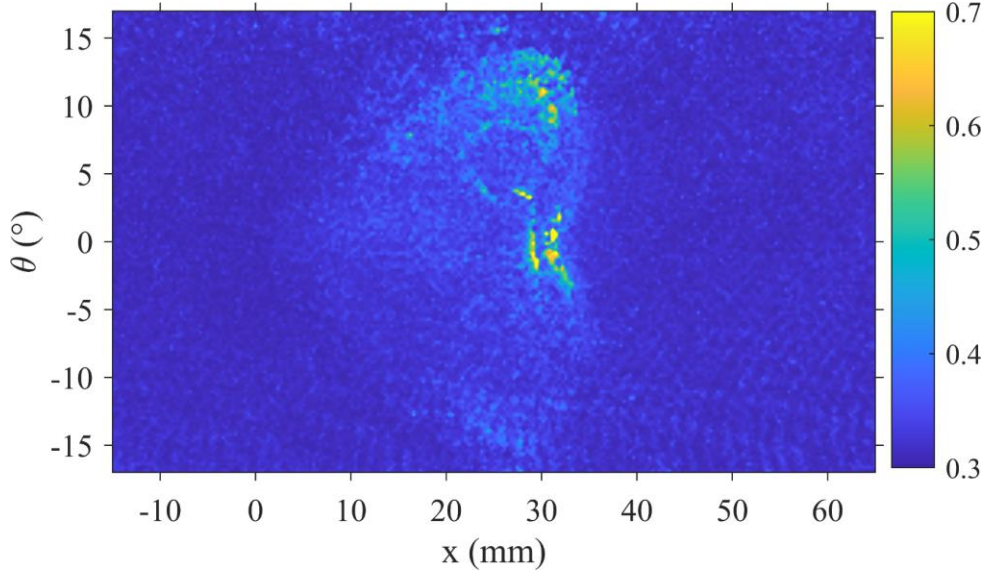


Figure 19: Uncertainty in the internal wall temperature

2. Bulk temperature uncertainty

One of the terms required for the calculation of the heat transfer coefficient is the bulk temperature T_b . As mentioned before, the temperature at each axial position is obtained by interpolating the temperature values measured at the center of the inlet and outlet section. Considering that the difference between these sections is around 0.17 K, the uncertainty is estimated as the thermocouple measurement uncertainty, 0.08 K. The sensitivity of the bulk is calculated as:

$$S_{T_b} = \frac{\partial Nu}{\partial T_b} = \frac{\partial Nu}{\partial h} \frac{\partial h}{\partial T_b} \quad (20)$$

3. Outer wall temperature uncertainty

The outer wall temperature, $T_{w,out}$, is measured by the IR camera to define the temperature potential in the heat conduction equation (Eq. 4). The uncertainty resulted from the IR camera can be calculated as in the internal wall temperature. For the overall external wall temperature, the systematic and random uncertainties are calculated at around 0.24 K and 0.11 K, respectively. To define the contributions of its systematic and random uncertainties, the sensitivity of $T_{w,out}$ is calculated as:

$$S_{T_{w,out}} = \frac{\partial Nu}{\partial T_{w,out}} = \frac{\partial Nu}{\partial h} \frac{\partial h}{\partial q_{conv}} \frac{\partial q_{conv}}{\partial q_{cond}} \frac{\partial q_{cond}}{\partial T_{w,out}} \quad (21)$$

4. Pipe thickness uncertainty

Since the heat conduction from the wall is resolved for each pixel element, a thickness map, $l(x,\theta)$, is generated by 3D scanning of the test section. the random uncertainty in the thickness is due to the accuracy of the scanning progress (± 0.01 mm), whose sensitivity is defined as:

$$S_{T_{w,out}} = \frac{\partial Nu}{\partial l} = \frac{\partial Nu}{\partial h} \frac{\partial h}{\partial q_{conv}} \frac{\partial q_{conv}}{\partial q_{cond}} \frac{\partial q_{cond}}{\partial l} \quad (22)$$

5. Thermal conductivity of the pipe and working fluid (air)

The errors in thermal conductivity values propagate the uncertainty bands of Nusselt number via conduction and convection heat transfer terms. The random uncertainty in the thermal conductivity of the pipe material (transparent ABS-like polyurethane) is estimated as % 1 of the measured value and its sensitivity can be calculated as;

$$S_{k_p} = \frac{\partial Nu}{\partial k_p} = \frac{\partial Nu}{\partial h} \frac{\partial h}{\partial q_{conv}} \frac{\partial q_{conv}}{\partial q_{cond}} \frac{\partial q_{cond}}{\partial k_p} \quad (23)$$

On the other hand, in the postprocessing, the thermal conductivity of the air is computed by the correlation proposed by Stephan and Laesecke [23] for air at atmospheric pressure with a standard deviation of 1.1%. Therefore, the uncertainty is a combination of the random uncertainty ($s_{k_{air}}$) due to the fit error and the systematic uncertainty due to the errors in measuring the bulk temperature ($b_{k_{air}}$) which is found by $b_{k_{air}} = b_{T_b} (\partial k_{air} / \partial T)$.

Pixel-by-pixel calculated sensitivities of Nusselt number to each measured source in the flow regimes of $Re=20k, 30k$ and $55k$ are respectively presented in Figure 20, 21 and 22.

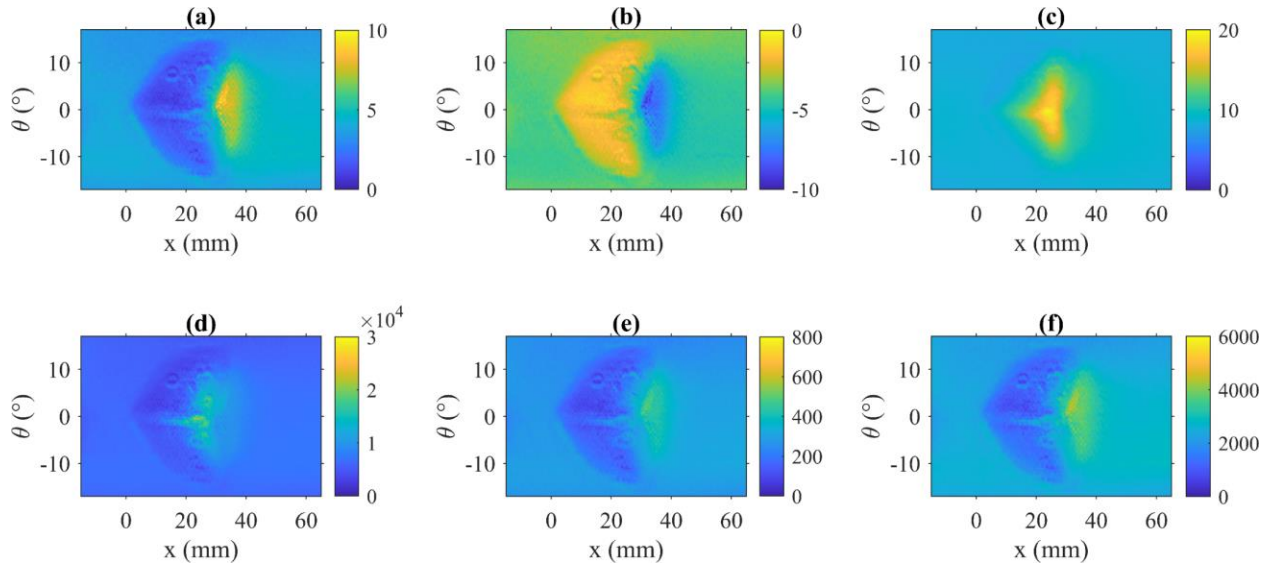


Figure 20: Sensitivities of the overall uncertainty to (a) the internal wall temperature [1/K], (b) bulk temperature [1/K], (c) outer wall temperature [1/K], (d) pipe thickness [1/mm], (e) thermal conductivity of the pipe [mK/W] and (f) the thermal conductivity of the air [mK/W]

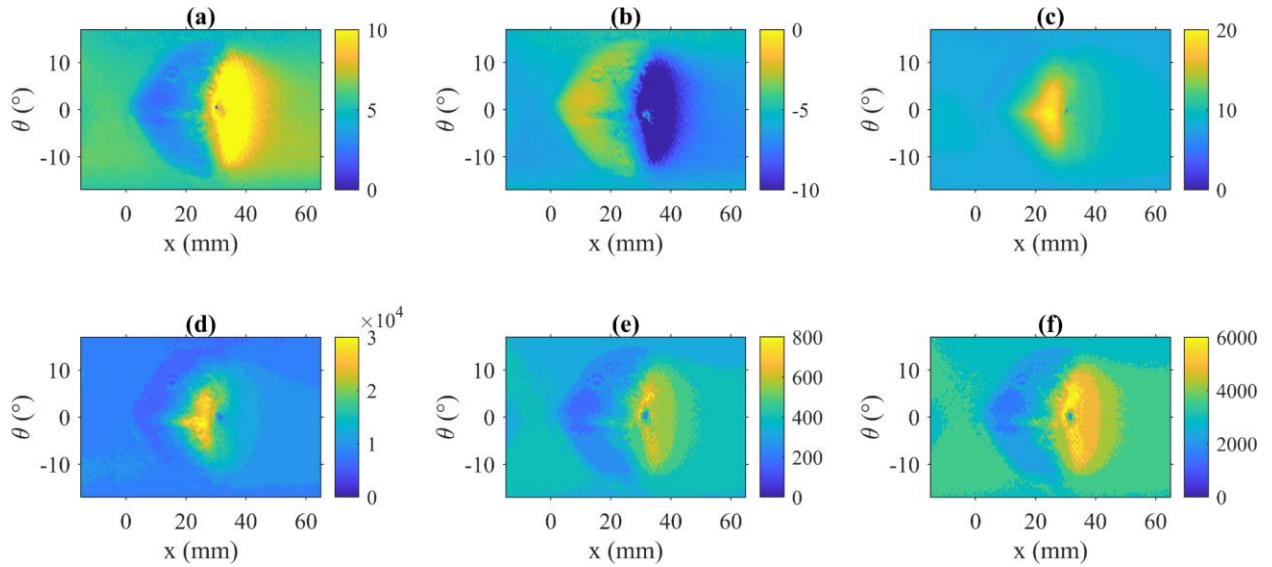


Figure 21: Sensitivities of the overall uncertainty to (a) the internal wall temperature [1/K], (b) bulk temperature [1/K], (c) outer wall temperature [1/K], (d) pipe thickness [1/mm], (e) thermal conductivity of the pipe [mK/W] and (f) the thermal conductivity of the air [mK/W] for the flow regime $Re=30000$

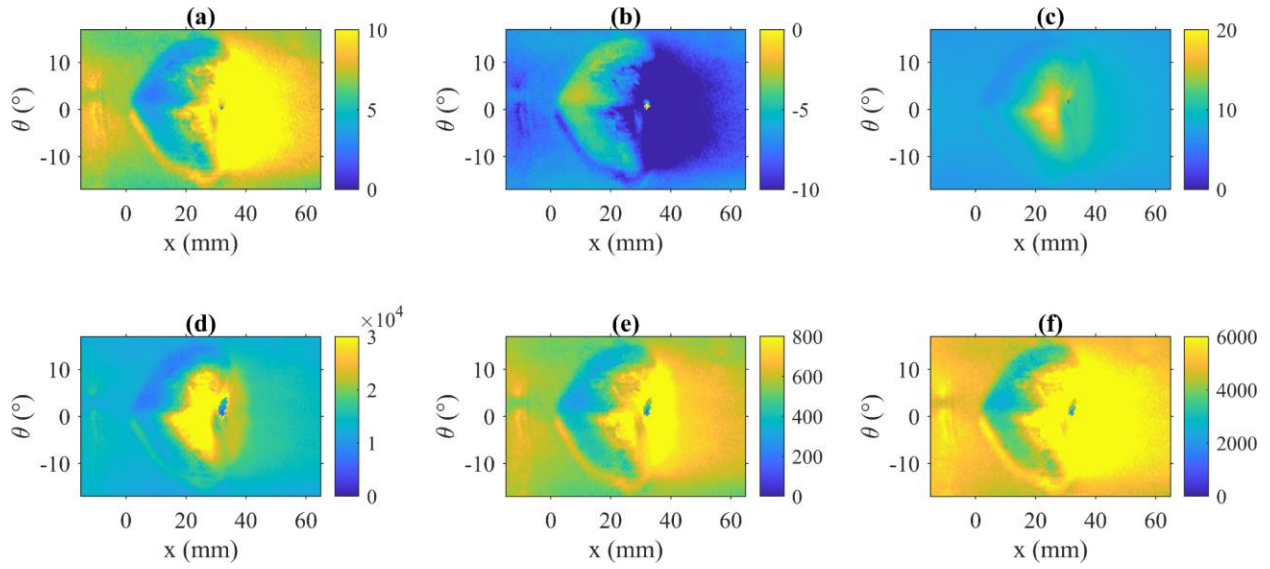


Figure 22: Sensitivities of the overall uncertainty to (a) the internal wall temperature [1/K], (b) bulk temperature [1/K], (c) outer wall temperature [1/K], (d) pipe thickness [1/mm], (e) thermal conductivity of the pipe [mK/W] and (f) the thermal conductivity of the air [mK/W] for the flow regime $Re=50000$

Finally, Figure 23 shows the overall uncertainties, defined at a confidence level of 95%, for the flow regimes of $Re=30k$ and $55k$.

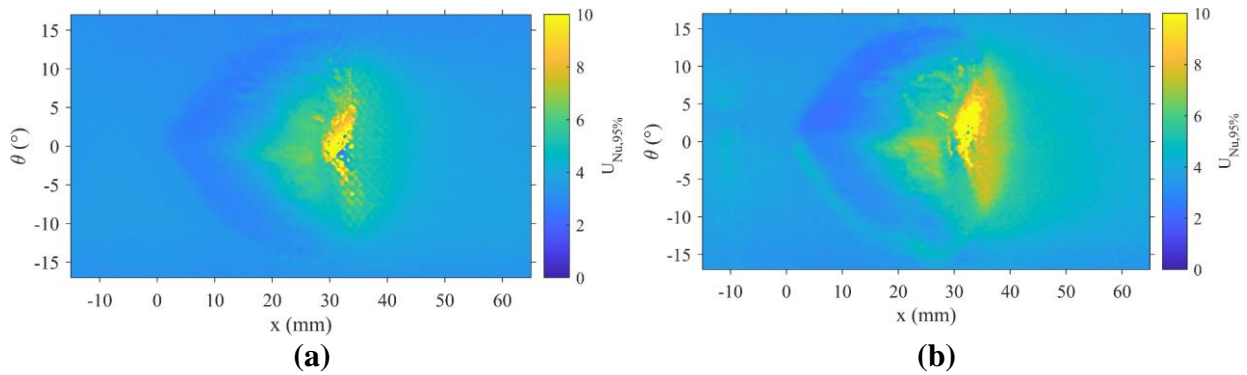


Figure 23: The expanded overall uncertainty in Nu field for the flow regimes of $Re=30000$ (a) and $Re=50000$ (b) around region of interest

Declaration of Competing Interests

The authors do not have any financial or non-financial interests to disclose.

Author contributions

M. C. Akkurt: Conceptualization, Formal analysis, Investigation, Resources, Methodology, Data curation, Project administration, Software, Writing - original draft, Writing - review & editing, Visualization. M. Virgilio: Conceptualization, Writing – review. T. Arts: Writing – review. K.M. Van Geem: Conceptualization, Resources, Supervision, Writing – review, Project administration, Funding acquisition. D. Laboureur: Conceptualization, Investigation, Methodology, Resources, Project administration, Software, Supervision, Writing – review.

Acknowledgments (Funding Information)

This research is funded by the European Research Council under the European Union's Horizon 2020 research and innovation programme / ERC grant agreement no 818607.

References

- [1] P. Ligrani, M. Oliveira, T. Blaskovich, Comparison of heat transfer augmentation techniques, *AIAA Journal* 41 (3) (2003) 337-362. <https://doi.org/10.2514/2.1964>
- [2] J. N. Dedeysne, M. Geerts, P. Reyniers, F. Wéry, K. Van Geem and G. Marin, computational fluid dynamics-based optimization of dimpled steam cracking reactors for reduced CO₂ emissions, *Transport Phenomena and Fluid Mechanics* 66 (8) (2020) 071702. <https://doi.org/10.1002/aic.16255>
- [3] V. N. Afanasyev, Y. P. Chudnovsky, A. I. Leontiev, P. S. Roganov, Turbulent flow friction and heat transfer characteristics for spherical cavities on a flat plate, *Experimental Thermal and Fluid Science* 7 (1993) 1–8.
- [4] N. K. Burgess and P. M. Ligrani, Effects of dimple depth on channel nusselt numbers and friction factors, *Journal of Heat Transfer* 127 (2005) 839–847.
- [5] Y. Rao, P. Zhang, Y. Xu, H. Ke, Experimental study and numerical analysis of heat transfer enhancement and turbulent flow over shallowly dimpled channel surfaces, *International Journal of Heat and Mass Transfer* 160 (2020) 120195. <https://doi.org/10.1016/j.ijheatmasstransfer.2020.120195>
- [6] Y. Xie, H. Qu, D. Zhang, Numerical investigation of flow and heat transfer in rectangular channel with teardrop dimple/protrusion, *International Journal of Heat and Mass Transfer*, 84 (2015) 486-496. <https://doi.org/10.1016/j.ijheatmasstransfer.2015.01.055>
- [7] Y. Chen, Y.T. Chew, B.C. Khoo, Enhancement of heat transfer in turbulent channel flow over dimpled surface, *International Journal of Heat and Mass Transfer* 55 (25-26) (2012) 8100– 8121. <https://doi.org/10.1016/j.ijheatmasstransfer.2012.08.043>
- [8] W. Zhou, Y. Rao, H. Hu, An experimental investigation on the characteristics of turbulent boundary layer flows over a dimpled surface. *J Fluids Eng* 138 (2) (2016) 021204–021217. <https://doi.org/10.1115/1.4031260>

- [9] R.S. Bunker, K.F. Donnellan, Heat transfer and friction factors for flows inside circular tubes with concavity surfaces, *Journal of Turbomachinery* 125 (4) (2003) 665–672.
- [10] M. Virgilio, J.N. Dedeyne, K.M. Van Geem, G.B. Marin, T. Arts, Dimples in turbulent pipe flows: experimental aerothermal investigation, *International Journal of Heat and Mass Transfer* 157 (2020) 119925. <https://doi.org/10.1016/j.ijheatmasstransfer.2020.119925>
- [11] F. Martins, C. Carvalho da Silva, C. Lessig, K. Zhringer, Ray-tracing based image correction of optical distortion for piv measurements in packed beds. *J Adv Opt Photonics* 1 (2018) 71–94. <https://doi.org/10.32604/jaop.2018.03870>
- [12] M.C. Akkurt, M. Virgilio, T. Arts, K. Van Geem, D. Laboureur, Ray tracing-based PIV of turbulent flows in roughened circular channels. *Exp Fluids* 63 (2022). <https://doi.org/10.1007/s00348-022-03529-z>
- [13] I. Mayo, B. C. Cernat, M. Virgilio, A. Pappa, and T. Arts, Experimental investigation of the flow and heat transfer in a helically corrugated cooling channel, *Journal of Heat Transfer* 140 (7) (2018) 071702. <https://doi.org/10.1115/1.4039419>
- [14] S.R. Sargent, C.R. Hedlund, P.M. Ligrani, An infrared thermography imaging system for convective heat transfer measurements in complex flows. *Meas Sci Technol* 9 (12) (1998) 1974–1981. <https://doi.org/10.1088/0957-0233/9/12/008>
- [15] B. Cukurel, C. Selcan, T. Arts, Color theory perception of steady wide band liquid crystal thermometry, *Experimental Thermal and Fluid Science* 39 (2012) 112–122. <https://doi.org/10.1016/j.expthermflusci.2012.01.015>
- [16] M. Virgilio, I. Mayo, J. Dedeyne, K. Van Geem, G. Marin, T. Arts, Influence of obstacles on the wall heat transfer for 2D and 3D helically ribbed pipes, *International Journal of Heat and Mass Transfer* 148 (2019) 119087. <https://doi.org/10.1016/j.ijheatmasstransfer.2019.119087>
- [17] R. Wiberg and N. Lior, Errors in thermochromic liquid crystal thermometry, *Review of Scientific Measurements* 75 (9) (2004) 2985-2994. <https://doi.org/10.1063/1.1777406>
- [18] I. Mayo, M. Virgilio, B.C. Cernat, T. Arts, Measurement uncertainty in liquid crystal thermography applied to internal cooling research: two practical examples, *Turbo Expo: Power for Land, Sea, and Air* (2018) GT2018-76361. <https://doi.org/10.1115/GT2018-76361>
- [19] M. Mendez, M. Raiola, A. Masullo, S. Discetti, A. Ianiro, R. Theunissen, J.-M. Buchlin, Pod-based background removal for particle image velocimetry, *Experimental Thermal and Fluid Science*, 80 (2017) 181-192. <https://doi.org/10.1016/j.expthermflusci.2016.08.021>
- [20] A. Sciacchitano, B. Wieneke, PIV uncertainty propagation, *Measurement Science and Technology* 27 (8) (2016) 084006. <https://doi.org/10.1063/1.555749>
- [21] A. Sciacchitano, Uncertainty quantification in particle image velocimetry, *Measurement Science and Technology*, 30 (2019) 092001. <https://doi.org/10.1088/1361-6501/ab1db8>
- [22] ASME PTC 19.1-2013, Test Uncertainty, American Society of Mechanical Engineers, New York, 2005.
- [23] K. Stephan and A. Laesecke, The thermal conductivity of fluid air, *J. Phys. Chem. Ref. Data* 14 (1) (1985) 227-234. <https://doi.org/10.1063/1.555749>
- [24] K. Zheng, W. Tian, P. Zhang, Y. Rao, H. Hu, Experimental Study of Turbulent Flow and Heat Transfer Behaviors Over a Micro-Rib-Dimple-Structured Surface. *ASME. J. Turbomach.* October 2021; 143 (10) (2021) 101014. <https://doi.org/10.1115/1.4050946>

[25] S. W. Churchill and H. H. S. Chu, Correlating Equations for Laminar and Turbulent Free Convection from a Horizontal Cylinder. *Int. J. Heat Mass Transfer* 18 (1975) 1049.

[26] F. P. Incropera, D. P. DeWitt, *Fundamentals of Heat and Mass Transfer* New York City, New York: John Wiley & Sons, Inc. (1996)

[27] S.B. Pope, *Turbulent Flows*, Cambridge-University Press, New York, 2000.